Energetic electron enhancements under radiation belt (L < 1.2) during nonstorm interval on August 1, 2008

Alla V. Suvorova [1,3], Alexei V. Dmitriev[2,3], and Vladimir A. Parkhomov[4]

[1] GPS Science and Application Research Center, National Central University, Jhongli, Taiwan
[2] Institute of Space Science, National Central University, Jhongli, Taiwan
[3] Skobeltsyn Institute of Nuclear Physics, Lomonosov Moscow State University, Moscow, Russia
[4] Baikal State University, Irkutsk, Russia

Correspondence to: Alla Suvorova (suvorova_alla@yahoo.com)

Abstract

An unusual event of deep injections of >30 keV electrons from the radiation belt to low L shells (L <1.2) in midnight-dawn sector occurred during nonstorm conditions on August 1, 2008. Using THEMIS observations in front of the bow shock, we found transient foreshock conditions and rotational discontinuities passing the subsolar region at that time. These conditions resulted in generation of fast magnetosheath plasma jets and penetration of the magnetosheath plasma into the magnetosphere as were observed by the THEMIS probes after approaching the magnetopause. The magnetosphere responded to variations in the IMF orientation by magnetic field perturbations. Magnetic records at ground-magnetometers of INTERMAGNET provided evidence of a global geomagnetic response in the form of geomagnetic pulses from the equator to middle latitudes. The earliest response was found at low latitudes in the predawn sector. We propose a scenario of possible association between dynamical foreshock in the subsolar region, magnetosheath plasma jets and the deepest injections of the >30 keV electrons at L < 1.2 at the midnight-dawn sector.

Key words: trapped energetic electrons, low L-shell, magnetosheath plasma jet, foreshock

1. Introduction

Deep injections of tens to hundreds of keV particles into the inner magnetosphere, i.e. drift shells L < 6, during quiet geomagnetic conditions or weak storm activity have recently become one of the main issues of radiation belt dynamics (e.g., Turner et al., 2017a; Zhao et al., 2017a). The cause of "quiet" injections has not been understood yet. An injection depth is estimated using a notion of drift L-shell, defined by McIlWain (1961). The L parameter determines the unique drift shell, which remains constant when a charged particle moves adiabatically in the inner magnetosphere. Numerically, L gives the average geocentric distance to a drift shell at the magnetic equator. Injection or transport of particles implies violation of adiabatic motion and changing of L-shell.

The mechanisms responsible for the violation of adiabatic motion of energetic particles are a subject of extensive modern studies of the radiation belts (e.g., Turner et al., 2015; Turner et al., 2017b; Zhao and Li, 2013; Zhao et al., 2016; Zhao et al., 2017a). The studies presented some intriguing challenges for current models of energetic particle injections in L-shell range of 2-6. Particularly it was pertaining to discrepancy in occurrence frequency, energy range, local time and penetration depth of electron versus proton injections. Zhao et al. (2016) showed that the electrons penetrate into the low L-shells more frequently than protons. In addition, it was found that tens to hundreds of keV electrons penetrate deeper than MeV energy electrons (e.g., Zhao and Li, 2013; Zhao et al., 2016). It was also found that energetic electrons can often penetrate down to the slot region separating the inner and outer radiation belts (L ~ 2.5 - 3.5) and also into the inner radiation belt at L < 2. Moreover, the deepest penetrations of energetic electrons were revealed even under the inner radiation belt at L < 1.2 (Asikainen and Mursula, 2005; Evans, 1988; Suvorova et al. 2012; 2013).

In the recent study, Zhao et al. (2017a) have compared local time characteristics of electron and proton flux enhancements in the slot region and suggested that underlying physical mechanisms responsible for deep penetrations of protons and electrons are different. Particularly, deep proton penetration is consistent with convection of plasma sheet protons, and deep electron penetration suggests the existence of a local time localized mechanism. Turner et al. (2015) studied energetic electron flux enhancements at L < 6 and also suggested that the deep injections at L < 4 (inside the plasmasphere) may result from a different mechanism than injections observed at higher L shells (outside the plasmasphere). They hypothesized that the mechanism could be related to wave activity in the Pi2 frequency range which usually serves as an indicator of substorm activity. Overall, dynamics of the tens to hundred keV electrons at low L-shells is very different from dynamics of both protons and electrons at higher L-shells and also in higher energy range.

The ability of energetic electrons to penetrate deeply in the inner zone and below is still puzzling. An answer to the question may be found by investigating the relation of deep injections of energetic electrons to solar wind parameters, geomagnetic activity indices and other parameters of magnetospheric and ionospheric responses (Suvorova, 2017; Zhao et al., 2017b). The studies mentioned above have reported deep injections of energetic electrons associated with geomagnetic storms and/or intense substorms, although no significant dependence of penetration depth or flux intensity on the storm intensity was found (e.g., Suvorova et al., 2013; 2014; Turner et al., 2017b; Zhao et al., 2016). Some studies noted that deep injections can occur during nonstorm time but under intense substorm activity (Park et al., 2010; Suvorova et al., 2016; Turner et al., 2015).

Extensive studies of dynamics of the energetic electrons in the inner radiation belt and below using the measurements from several satellite missions NOAA/POES, DMSP, DEMETER, and Van Allen Probes (e.g., Reeves et al., 2016; Suvorova, 2017; Turner et al., 2015, Turner et al., 2017a; Zhao and Li, 2013; Zhao et al., 2017a) have revealed the following interesting features such as a high growth rate of fluxes or sudden enhancements, the occurrence of flux enhancements regardless of storm intensity, the influence of solar wind and geomagnetic conditions on the occurrence rate, high occurrences of the injections below the inner zone during specific phases of solar cycles, specific months and local times.

Rapid enhancements of electron fluxes in the inner zone have been known for a long time in association with deep injections of particles during strong magnetic storms (e.g., Pfitzer and Winckler, 1968; Imhof et al. 1973; Kikuchi and Evans, 1989; Tanaka et al., 1990). As mentioned, recent studies showed that rapid or sudden enhancements deep in the inner magnetosphere cannot be explained by an enhanced convection electric field, convection of plasma sheet electrons or inward radial diffusion (e.g., Turner et al., 2017b; Zhao et al., 2017a). Increased statistics have revealed a feature that deep injections may occur frequently, and furthermore, regardless of storm strength (Tadokoro et al., 2007; Park et al., 2010; Turner et al., 2017a; Zhao and Li, 2013; Zhao et al., 2016). Another important feature, also mentioned above, is that injections of the keV electrons and associated flux enhancements can occur even below the inner belt edge (L ~ 1.2), in so-called forbidden zone (Asikainen and Mursula, 2005; Evans, 1988; Suvorova et al., 2012).

Until recent years, it was believed that these “forbidden injection” events could occur only during strong magnetic storms and hence could be rarely observed. Note that enhancements in the forbidden zone were first reported in 1960s (Krasovskii et al., 1961; Savenko et al., 1962; Heikilla, 1971), however, the conclusions were unconvincing due to the scarce information (see Paulikas, 1975 for a review). The recent statistical study of electron enhancements in the forbidden zone showed that the injections below the inner zone can also occur during geomagnetically quiet conditions (Suvorova, 2017). This fact is consistent with the recent finding of “quiet” injections in the inner magnetosphere (Turner et al., 2017a; Zhao et al., 2017a). A case of “quiet” injections of energetic electrons at $L < 1.2$ is in the focus of our study.

Here, we summarize the main characteristics of the electron injections into the very low L-shells from several papers (Suvorova and Dmitriev, 2015; Suvorova et al., 2013; 2014; 2016; Suvorova, 2017; Dmitriev et al., 2017). The quasi-trapped energetic electron population in the forbidden zone, referred to as forbidden energetic electrons (FEE), can be characterized as transient with highly variable fluxes. The behavior of FEE is similar to keV energy trapped electrons in the inner radiation belt with flux enhancements in response to magnetic storms (e.g., Kikuchi and Evans, 1989; Tanaka et al, 1990; Tadokoro et al., 2007; Dmitriev and Yeh, 2008; Zhao and Li, 2013; Selesnick et al., 2016). Simultaneous measurements of particles by satellites at different altitudes provided clear evidence that the forbidden zone enhancements of energetic electrons were caused by fast penetration of the inner belt electrons (Suvorova et al., 2014). As known, an important role in fast transport of particles during storms is played by magnetic and electric field perturbations. Such perturbations are usually associated with the influence of magnetospheric substorms, or nighttime processes of magnetic field dipolarizations in the magnetotail (e.g., Glocer et al., 2011; Selesnick et al., 2016). However, substorm signatures in the magnetic field in the low-L region (L< 2) have never been observed.

Thus, the deep injections of keV energy electrons may extend even to the forbidden zone, but conditions for the fast (~1 - 2 h) earthward transport in the low-*L* region are still unclear. Nevertheless, the most probable mechanism of the low-*L* injections of energetic electrons was suggested as the *ExB* drift (e.g., Suvorova et al., 2012), and most of researchers consider and model an electric drift of electrons in the ExB fields, even though the electric field must be very high (e.g., Zhao and Li, 2013; Turner et al., 2015; Lejosne and Mozer, 2016; Selesnick et al., 2016; Su et al., 2016; Zhao et al., 2017a). According to simulation results of Selesnick et al. (2016), the electric field of ~5 mV/m can provide deep injections at L<1.3. There is no explanation for penetration of a strong electric field to such low *L*-shells. What is more important, there is no reliable information on electric fields at heights of 500-2000 km, because measurements there are difficult, and, as a consequence of this, empirical electric field models are limited and do not provide the results below L~2 (e.g., Rowland and Wygant, 1998; Matsui et al., 2013). The most modern research suggests that the actual strength of penetration electric fields can be stronger than any existing electric field model at L < 2 (Su et al., 2016).

The studies, mentioned above, have also analyzed a relation between the FEE injections and geomagnetic activity level. It seemed for a while that intense geomagnetic activity like auroral substorms was one of the necessary factors for deep electron injections, and the storm-time *Dst*-variation did not control the FEE occurrences (Suvorova et al., 2014). It was suggested that substorm-associated strong electric field can penetrate to the low *L* region, thereby creating the conditions for fast earthward transport of trapped electrons in crossed E and B fields. Recent modeling of the ExB transport mechanism at $L < 1.3$ demonstrated that the mechanism can successfully operate in the low *L* region (Selesnick et al., 2016).

However, after that, many FEE events were found during moderate and weak auroral activity, which was typical for pre-storm (initial phase) or even non-storm conditions (Suvorova and Dmitriev, 2015; Suvorova et al., 2016). Thus, though no evidence of direct influence of geomagnetic storms was found, the FEE enhancements appeared to be necessarily associated with substorm activity in some events studied (Suvorova et al., 2014; 2016). However, statistically, such a casual relationship with substorms was not confirmed (Suvorova, 2017). From total statistics of ~530 days with FEE enhancements collected during two solar cycles (Suvorova, 2017), we found more than three dozen days without essential substorm activity. These “quiet” events occurred over past decade from 2006 to 2016. The FEE enhancements in that case were observed only in low energy range of tens of keV.

It is important to mention that one interesting feature was unexpectedly found from the statistical study (Suvorova, 2017). It is that the most favorable conditions for the FEE enhancements arise in the period from May to September independently on geomagnetic activity level. A second, minor peak of occurrence appears in the December - January period. Suvorova (2017) suggested an important role of the auroral ionosphere in the occurrence of FEE injections. The peculiar annual variation of the FEE occurrence rate was explained by a change in conductance of the auroral ionosphere. The conductance depends directly on the illumination of the noon sector of the auroral zone. As known, the high-latitude ionosphere is better illuminated during solstice periods, with that the illumination of the northern region is higher than the illumination of the southern one because of the dipole axis offset relative to the Earth’s center. This fact can explain an existence of two peaks of the FEE occurrence with the major one during the northern summer period.

External drivers from the solar wind should trigger some processes in the magnetosphere-ionosphere system that might result in the electron injections into the forbidden zone. However, the external drivers are necessary but often not sufficient for FEE enhancements to occur. If the auroral ionosphere is sunlit, then impact of external drivers more likely results in the electron injections into the forbidden zone. In this case, the factor of the dayside auroral ionosphere conductivity is sufficient, and it comes to the fore during weak geomagnetic activity. The relevant processes in the magnetosphere-ionosphere chain during magnetic quiet are still unclear. A comprehensive analysis of the solar wind drivers and magnetospheric response may help us to lift the veil. In this paper, we study prominent FEE enhancements during nonstorm condition on August 1, 2008 in order to determine their possible drivers in the solar wind. Note that this event is a subset (1%) of the total statistics collected by Suvorova (2017) during various conditions, from magnetic quite to extremely strong geomagnetic storms.

2. Observations on August 1, 2008

2.1. Forbidden Electron Enhancements

Figure 1 shows large enhancements of the >30 keV electron fluxes at low latitudes on August 1, 2008. The data were compiled from all orbital passes of five NOAA/POES satellites. The electron fluxes in the energy ranges >30, >100 and >300 keV were measured by the MEPED instruments boarded on each satellite. The MEPED instrument includes two identical electron solid-state detector telescopes and measures particle fluxes in two directions: along and perpendicular to the local vertical direction (Evans and Greer, 2004). The data shown in Figure 1 are from the detector was oriented along the orbital radius-vector (i.e. vertically), so that it measured quasi-trapped particles near the equator and precipitating particles in the auroral region. In Figure 1, the forbidden zone extends at $L < 1.2$ in the latitudinal range from -20° to +30° and in the longitudinal range from 0° to 260°E (or 100°W) that is beyond the South Atlantic anomaly (SAA). Figure 1a shows the observations of the >30 keV electrons at 0 - 12 UT, before the enhancements occurred. At that time, the satellites passed the same regions but they did not detect any FEE enhancements. Figure 1b shows the interval 12 - 24 UT, when fluxes of >30 keV quasi-trapped electrons in the forbidden zone increased by 3 orders of magnitude above a background of ~10^2 (cm^2 s $sr)^{-1}$. We have selected FEE enhancements with intensity >10^3 (cm^2 s $sr)^{-1}$. As found previously, the flux enhancements at low latitudes are peculiar to the quasi-trapped energetic electrons (Suvorova et al., 2012, 2013). In contrast, enhancements of electrons precipitating at low latitudes are very rare, weak and short. During the event, precipitating electron fluxes in the forbidden zone did not increase (not shown). Fluxes of the >100 keV electrons and >30 keV protons did not increase also (not shown). The quasi-trapped electrons are mirroring at heights below the satellite orbit (~850 km) in a region of ±30° latitudes, and drift eastward with a rate of 17°-19° per hour toward the SAA area, where they are lost due to scattering in the dense atmosphere.

Figure 2 and Table 1 present main characteristics of 15 FEE enhancements detected along equatorial passes of POES satellites (P2, P5, P6, P7, P8). The fluxes kept at the enhanced level for several hours. We analyze the peak fluxes in the FEE enhancements (time, local time, longitude, and L-shell). Positions of the satellite orbital planes provided a good coverage of the entire local time (LT) range: 9 - 21 LT (P2 and P7), 5 - 17 LT (P5 and P6), and 2 - 14 LT (P8). The coverage allows determining the injection region with uncertainty of approximately 2 h. The first FEE enhancement was observed at ~1250 UT in Central Pacific at night time (2 LT), and the last (enhancement number F15) was detected at ~2310 UT near the western edge of SAA at day time (17 LT). As seen in Figure 2a,b, the FEE enhancements peak at minimal L-shells, i.e. at the equator. The fluxes decrease quickly with growing L. This pattern corresponds to a fast radial transport (injection) of electrons from the inner radiation belt. Note that pitch-angular scattering of electrons gives different profiles: the fluxes should be minimal and the equator and grow with L-shell.

It was shown statistically that deep injections into the forbidden zone, similar to plasma sheet particle injections, occur in the midnight - morning sector (e.g., Suvorova, 2017). During typical geomagnetic disturbances, nighttime FEE enhancements are observed shortly after local injections and near an injection site, while subsequent FEE enhancements at daytime are already the result of azimuthal drift of electrons injected on the nightside. Hence, the nighttime (~2 LT) enhancements F1 and F4 of >30 keV electron fluxes indicate approximately the time of injection, respectively, at ~1250 and ~1430 UT or a little bit earlier. After 1530 UT, enhancements were observed at daytime (numbers F7, F9, and F11-15) and are therefore associated with drifting electrons.

All remaining enhancements F2, F3, F5, F6, F8 and F10 of >30 keV electron fluxes were observed in the early morning (5 LT) for a long time interval of ~4 h that lead us to suspect that the enhancements were observed near the injection site. Nevertheless, we examine the assumption about drift by comparing these enhancements with the injection time for numbers 1 and 4 in Table 1. For the enhancements F1 and F2, 30 keV electrons injected at 1250 UT must drift ~35.4° of longitude in order to reach the observing satellite P5. It takes ~112 min with the drift rate of 19°/h for 30 keV electrons at L~1.2 or 125 min with the drift rate of 17°/h at L~1.1. However, the observed time difference between F1 and F2 is only 25 min that is too short for drifting from the longitude of F1 to the longitude of F2.

The enhancements F1 and F3 have the longitudinal difference of 26° for 1 h that is much larger than 19° produced by the drift of >30 keV electrons. Either it could be electrons of slightly higher energy of ~40-50 keV. However, intensity of these electrons is several times lower than that for 30 keV electrons because of very steep energy spectrum with maximum in the range of 20-30 keV as shown in the previous study (Suvorova et al., 2013). In contrast, the observations did not show notable flux decrease. It means that vast majority of the POES/MEPED count rate is produced by electrons of ~30 keV.

Likewise, one can infer that the enhancement F4 also did not result in the enhancements F5 and F6 and certainly not in the enhancements F8 and F10. Therefore, the specific longitudinal and local time distributions of the enhancements indicate multiple injections during about 4.5 h in the sector of 0 - 6 LT, and the injection region was confined within 3 h of local time over central and eastern Pacific. In general, these characteristic of injections are in well agreement with those found from statistics (Suvorova, 2017).

2.2. Upstream Solar Wind Conditions

An intriguing aspect of these FEE injection events is that they occurred under quiet, nonstorm conditions, characterized by Dst/SYM-H ~ 0 nT and AE < 100 nT. We examine solar wind parameters to search for drivers inducing such deep electron injections. In the study, we focus on a comparison between the solar wind parameters measured far upstream and near the bow shock and on their influence on the magnetospheric magnetic field during the period of interest. Global indices of geomagnetic activity and solar wind data from the Omni high-resolution data set are shown in Figure 3. The OMNI data base provides solar wind data, which were originally obtained from upstream monitors (e.g., ACE or Wind satellites) near the L1 libration point at geocentric distance of ~230 Re (Re is the Earth's radius), and then the data were corrected by time delay procedure due to propagation to the Earth's bow shock (King and Papitashvili, 2005).

As seen in Figure 3, the solar wind speed and density smoothly varied around averages of 400 km/s and 6 to 4 cm^{-3}, respectively, that resulted in gradual change of the dynamic pressure Pd from 2 to 1 nPa. The interplanetary magnetic field (IMF) can be characterized as weakly disturbed by small-scale structures because of chaotic variations of the magnetic field components and discontinuities, particularly during the fist half of the day. Also, in this period, the Bz component was predominately positive. Later, there was a short interval from 1500 to 1800 UT, when IMF orientation was relatively steady with a continuous negative Bz of about -2 nT. Likely, the southward IMF resulted in intensification of the *AL* index from 16 to 18 UT with a peak of -250 nT. The 1 min *SYM-H* index was > -10 nT throughout the whole day, indicating there was no geomagnetic storm. Therefore, the solar wind conditions resulted in a weak auroral disturbance like an isolated substorm.

Overall, the OMNI magnetic and plasma parameters can be characterized as almost undisturbed in the period of the FEE enhancements from 1200 to 2300 UT. Obviously, the weak auroral activity at ~1700 UT could not result in extremely deep injections of the energetic electrons, which started much earlier, around 1300 UT. Whereas, looking on the PC index, which represents magnetic activity in the northern (PCN) and southern (PCS) polar caps (Troshichev et al., 1988), one can see a clear disturbance, particularly in the northern polar cap, in the period from 1300 to 1530 UT. But it's difficult to identify appropriate solar wind drivers for interpretation of this polar cap activity.

This raises the question of actual solar wind characteristics at the near-Earth location during the event. The FEE enhancement event under the nonstorm condition and mild, ordinary solar wind properties presents intriguing challenge to current understanding of the deep energetic particle injections, which usually are associated with intense substorm activity. From the characteristic PC-index behavior, we suspect the actual solar wind parameters affecting the magnetosphere may be different from those predicted by OMNI. Fortunately, the near-Earth THEMIS mission can provide necessary reliable information on upstream conditions.

2.3. THEMIS foreshock observations

During the time interval from 1200 to 1800 UT, the THEMIS-C satellite (TH-C) had a position upstream of the bow shock in the subsolar region (Figure 4). The TH-C probe moved from location (17.2, -0.3, -5.9) Re in GSM at 1200 UT to location (18.1, 3.4, -5.9) Re at 1800 UT. Hence, we can evaluate characteristics of the upstream solar wind structures actually affecting the magnetosphere during the period of the FEE enhancements. Figure 5a shows measurements of the THEMIS-C/FGM fluxgate magnetometer in GMS coordinates with a time resolution of ~3 s (Auster et al., 2008) and the ion spectrograms from THEMIS-C/ESA plasma instrument (McFadden et al., 2008). The magnetic field components measured in situ by TH-C are compared with those predicted by OMNI and shown in Figure 5b. Also, Figure 5c presents the IMF cone angles, between the IMF vector and the Earth-Sun line, for both magnetic data sets.

From 1200 UT to 1320 UT, three TH-C magnetic components demonstrated small-amplitude variations, and the Bz component had northward direction. During this time, there were discrepancies between magnetic components of the TH-C and OMNI data caused mostly by time shift of ~10-15 min, so that TH-C observed arrival of the solar wind structures at earlier time than that predicted by OMNI. With time correction, one can achieve better consistency in the two magnetic data sets except the difference in the Bx components about 1310 UT.

In Figure 5c, the OMNI cone angle dropped below 30° between 1330 and 1520 UT that corresponded to quasi-radial IMF orientation (IMF is almost along the Earth-Sun line), whereas cone angle variations detected by TH-C were very different from the OMNI data. After 1500 UT, the OMNI data do not match the TH-C observation any more, even with time correction. About ~1320 UT, ~1400 UT and after 1440 UT, the in-situ observation of THEMIS shows large-amplitude fluctuations with duration of tens of minutes in three magnetic components and cone angle (Figure 5a, c). The observed large magnetic fluctuations are ultralow-frequency (ULF) waves, and they are a typical signature of the upstream region of quasi-parallel bow shocks, so-called foreshock (e.g., Schwartz and Burgess, 1991). In addition, in the same time intervals, the plasma spectrogram shows enhancements of suprathermal ion fluxes with energy of >10 keV (upper panel in Figure 5a). This is another distinguishing signature of the foreshock, known as diffuse ion population, which is always observed together with the upstream ULF waves

(Gosling et al., 1978; Paschmann et al., 1979; Greenstadt et al., 1980; Crooker et al. 1981). Hence, the upstream foreshock waves and diffuse ions observed by TH-C in the subsolar region are associated distinctly with a radial or quasi-radial IMF orientation in the undisturbed solar wind. Note, that the longest foreshock interval (1435 - 1550 UT) associated with the quasi-radial IMF orientation was observed by ~20 min later than that predicted by OMNI.

After 1520 UT, the prediction and in-situ data mismatch greatly. The TH-C satellite observed several rotational discontinuities and alternation between Archimedean spiral and radial orientations of the IMF vector, while the OMNI magnetic field does not change the Archimedean spiral orientation from 1520 to 1740 UT. The foreshock returned to the subsolar region periodically and more frequently in the interval 1600 - 1730 UT than in the earlier period 1320 - 1440 UT.

These two time intervals of frequent foreshock transitions differ in the Bz component: $B_z > 0$ at 1320 - 1440 UT and $B_z < 0$ at 1600-1700 UT. It's natural, that the southward Bz results in the weak auroral activity during the later interval. Nevertheless, the changing direction of IMF has the effect on the magnetic activity in the northern polar cap in the both interval (see the PC index in Figure 1). We check available satellite and ground-based magnetic data to find other responses inside the magnetosphere to the foreshock transitions.

2.4. Magnetospheric magnetic field perturbations

We use magnetic field and plasma measurements in the magnetosphere from the other three THEMIS probes and GOES-12 satellite in order to find signatures of local magnetospheric disturbances. With these data, we examine a magnetospheric response to the subsolar foreshock, which forms each time with arrival of magnetic flux tubes with quasi-radial IMF orientation. Positions of the TH-B, TH-D, TH-E and GOES-12 satellites in the X-Y GSM plane for the period from 1200 to 1800 UT are shown in Figure 4. We used the model of Lin et al. (2010) to calculate magnetopause position. The OMNI data at 1600 UT is used as input data for the model. The GOES12 satellite moved from morning to noon (7 - 13 LT). The TH-E and TH-D probes moved outward from prenoon to postnoon, and the TH-B probe moved inward in the afternoon-dusk sectors.

Figure 6 shows variations of the Bz component measured by the TH-E, TH-D, and TH-B probes, the magnetic field strength at geosyncronous orbit (GOES-12), the ion spectrogram from the TH-D satellite and the SYM-H index from 1200 to 1800 UT. As seen in Figure 6 (a, d), characteristics of magnetic field and hot plasma indicate that three THEMIS probes were located inside the dayside magnetosphere during the interval, a region of a strong magnetic field with the magnitude ranging from 40 to 150 nT and low-density of hot (>10 keV) ions. Three THEMIS probes observed significant perturbations in the magnetic field Bz component with increase/decrease of order of several to tens of nT. After 1400 UT, the largest amplitudes were observed by TH-D, which was closer to the magnetopause than other probes at that time (see Figure 4). From 1300 to 1500 UT, there are a few characteristic decreases and enhancements in the Bz component with duration of 20-30 min observed by all probes (Figure 6a). The magnetic field increases correspond to magnetospheric compressions, and the decreases are magnetospheric expansions (e.g., Dmitriev and Suvorova, 2012). Prominent magnetic peaks are indicated by dashed lines and listed in Table 2. At ~1700 and 1715 UT, the TH-D measurements show that the sign of the Bz component suddenly reversed for a few minutes. The negative Bz component is a clear signature of the magnetosheath magnetic field. We will consider details of the magnetosheath intrusion events later.

As seen in Figures 6a-c, THEMIS magnetic observations well correlate with magnetic field variation observed by GOES-12 and with the SYM-H index in the interval 1300-1600 UT. The first magnetic pulse was observed at ~13:33:40 simultaneously by TH-B, TH-E, and TH-D and with a delay of ~2 min by GOES 12. Time moments of magnetic peak 2 coincide for all satellites (14:20:50 UT). Magnetic peak 3 was observed at first by GOES 12 at ~15:44:00 (~10.6 LT), then by TH-E at ~15:47:30 (~12 LT) and at last by TH-D at ~15:50:30 UT (~12.5 LT), so a time difference between GOES 12 and TH-D is ~ 6.5 min and between TH-E and TH-D is 3 min.

The magnetic variations associated with compression-expansion effects could not be caused by the solar wind pressure variations, which were gradual and small during the interval (see Figure 3). However, the magnetic perturbations may result from local variations in the magnetosheath pressure. Unfortunately, THEMIS did not measure plasma parameters in the magnetosheath from 1200 to 1600 UT, but an analysis of the later interval (1600-1800 UT) can provide important information about magnetosheath conditions (see also section 2.5).

After 1545 UT, the TH-D probe observed fast magnetic variations. At that time the probe was approaching the magnetopause and moving ahead of the TH-E probe (see Figure 4). Note, that the fast magnetic fluctuations are not always seen in SYM-H and GOES 12 data because of a low time resolution (1 min) of these data. Figure 6d presents the ion spectrogram from TH-D. One can see several short-time intrusions of dense and cold plasma with spectrum typical for the magnetosheath. Moreover, at ~1700 and 1710 UT, the magnetospheric field measured by TH-D with positive Bz suddenly overturned to negative Bz for a moment that indicated a magnetosheath encounter. Time moments of peaks in the magnetosheath plasma pressure are indicated by lines 4-10 in Figure 6 and listed in Table 2. Below, we analyze characteristics of magnetosheath ions in details.

2.5. Magnetosheath plasma jets interacting with the magnetopause

We analyze the solar wind characteristics in the foreshock region together with the magnetospheric magnetic perturbations and penetration of magnetosheath ions. Figure 7 shows the magnetic field and plasma parameters observed by TH-D, TH-E and TH-C during the interval 1530-1800 UT. In addition, magnetic measurements from GOES 12 and geomagnetic indices are also shown.

After 1530 UT, the TH-D and TH-E probes have observed magnetic field pulses associated with the compression effect (Figure 7g). After 1600 UT, TH-D was approaching the magnetopause and started observing occasionally magnetosheath plasma in the magnetosphere, as seen in the ion spectrogram (e.g., lines #4 – 7 and 10, Figures 7b). After 1700 UT, the probe twice entered into and exited from the magnetosheath region as indicated by lines #8 and #9. The magnetosheath plasma can be recognized as dense and cold (<1 keV) ion population. As seen in Figure 7 (panels b and g), not all magnetic pulses are accompanied by plasma penetrations. During the interval, the outermost probe TH-C observed occasionally the foreshock phenomena such as diffuse ions (≥10 keV) in the spectrum (panel a) and large IMF cone angle fluctuations associated with ULF waves (panel h). As one can see, most of the magnetic pulses (panel g) and/or magnetosheath ion populations (panel b) indicated by lines #3, #4, and #6-10 (i.e. except #5) were accompanied by the foreshock diffuse ions (panel a).

Figure 8 shows characteristics of magnetosheath plasma in details for three intervals 1600-1630, 1630-1700, and 1658-1728 UT. Since plasma charge neutrality means equal density of ions and electrons, Figure 8 presents parameters of the ion component only (panels a-d). Total pressure (*P*tot) and density (*D*) of the solar wind plasma measured far upstream by the ACE monitor are also shown for comparison in panels (b, c). The time period from 1600 to 1630 UT is shown in panels (a1-g1). The probes TH-D and TH-E observed magnetic field variation in specific depletion-hump sequence from 1607 to 1614 UT (panels f1, g1), similar to the variations indicated by lines #1 - #3 in the earlier interval (see Figure 6). Magnetic peak is indicated by line #4. Additionally, wave-like structures with a period of ~30-60 sec (in the ULF range) are clearly seen in magnetic measurement of both probes during the time interval from 1609 to 1627 UT (panels f1, g1). At 1614 - 1616 UT, TH-D observed cold ions (~100 eV - 3 keV) and electrons (<1 keV, not shown) of the magnetosheath origin staying in the magnetosphere (panel a1). The plasma has maximal speed of >200 km/s and high density of 3-9 cm^{-3} that result in the high total pressure of 1.5 - 1.8 nPa (panels b1-d1). Its dynamical characteristics distinctly exceed the solar wind parameters with density of 4 - 5 cm^{-3} and total pressure of ~1.1 nPa (panels b1, c1). Internal structure of plasma forms 3 prominent pressure pulses between 16:14:50 and 16:16:00 UT, a central pulse is dominated by magnetic component (panel f1) and two lateral pulses are dominated by dense plasma components (panel c1). Two plasma density enhancements produced a diamagnetic effect seen as a characteristic decrease of magnetic field (panel f1). At the outer edge of the plasma structure, the anti-sunward velocity (Vx < 0) reached high value of -100 km/s, indicating that the local plasma flow struck and interacted with the magnetopause (panel d1). The Vz component demonstrates a maximal value in southward direction (-200 km/s). Three rotated velocity components Vx, Vy and Vz indicate that vortex-like plasma structure propagated along the magnetopause toward south and dusk. This dense and high-speed plasma structure is analogous to the large-scale magnetosheath plasma jet studied by Dmitriev and Suvorova (2012). Large-scale magnetosheath plasma jets are defined as intense localized fast ion fluxes whose kinetic energy density is several times higher than that in the upstream solar wind and duration is longer than 30 sec (Dmitriev and Suvorova, 2015).

Panels (a2-g2) in Figure 8 show magnetic compressions and magnetosheath penetrations (lines #5 - #7) during the time period from 1630 to 1700 UT. It is also seen that the magnetic field measured by TH-E was disturbed by ULF wave activity (panel g2). The plasma structures #5 and #6 (panel a2) have short durations and are characterized by extremely high density of 16 and 12 cm^{-3}, respectively, that well explain the compression effects in magnetic measurements from TH-E and TH-D (panels f2, g2). Prolonged plasma structure #7 has lower density of 4 - 9 cm^{-3} and did not produce a notable compression effect in accordance with to TH-E magnetic measurements (panel g2). It is important that inside each plasma structure, we reveal a dense plasma core, which is characterized by enhanced speed of ~150 or ~220 km/s with a dominant Vz component (negative or positive). These parameters, typical for plasma jets, formed pressure of high magnitude, which exceeded the upstream solar wind pressure by 50-80 % (panel b2). Likely, magnetosheath plasma jets interacted with the magnetopause, and then they were partially trapped thereby penetrating into the magnetosphere (Dmitriev and Suvorova, 2015). The amount of this penetrated plasma estimated by the authors can be comparable with estimates of the total amount of plasma entering the dayside magnetosphere (Sibeck, 1999).

During the last time period 1658 - 1728 UT shown in panels (a3-g3), we have an excellent opportunity to examine plasma parameters in the magnetosheath region adjacent to the magnetopause. Panels (a3-f3) show two cases of magnetopause distortions followed by short intervals of the magnetosheath from ~1700 to 1701 UT and from 1711 to ~1715 UT. The ULF wave activity is also clearly seen in the magnetic measurement of the TH-E probe (panel g3). The TH-D probe at distance of ~10.8 Re and ~13 LT suddenly crossed the magnetopause and moved into the magnetosheath, a region where the magnetic field vector rotated to negative Bz (panel f3). Plasma in both magnetosheath intervals has extremely high density (~20 cm^{-3}) and high velocity (≤ 200 km/s). In the magnetosheath, one can see local pressure pulses around ~1700 UT and ~1712 UT (lines #8 and 9). For #9 case, TH-E observed a small shallow hump of the magnetic field of a few nT between two depletions at 1707 and 1715 UT (panel g3). The last event (#10) shown in Figure 8c is a short penetration of magnetosheath plasma accompanied by a small perturbation in the magnetospheric field observed at ~1724-1725 UT (panels e3, f3). Density and pressure of this structure did not exceed the solar wind parameters, though the velocity was large (~150 km/s) with dominant negative Vz component (panel b3-d3).

Thus, we found typical characteristics of dense and fast plasma jets in all intrusions of the magnetosheath plasma into the magnetosphere and in the magnetosheath itself. Most of these structures caused local compression effects at the dayside. Also, the TH-E magnetic field is modulated by ULF waves in the range of magnetic pulsations Pc 3-4 with period between 10 and 60 seconds. As known, dayside Pc 3-4 waves are originated in the upstream solar wind and penetrate into the magnetosphere, while their amplitude is controlled by a foreshock position or IMF orientation (e.g., Guglielmi, 1974).

As shown in Figure 3, moderate auroral and polar cap activity was observed during the same time (1600-1800 UT). However, it should be noted that in the preceded interval 1300-1600 UT, associated with the deep electron injections and FEE enhancements, the THEMIS probes also observed similar magnetic compression-expansion effects at inner part of orbits (~7 - 10 Re). At that time, we found enhanced magnetic activity in the polar cap (only in the northern hemisphere), but no auroral activity. This raises an interesting question about spatial pattern of geomagnetic field response to the impact of magnetosheath pressure pulses/plasma jets interacting probably with the dayside magnetopause in the earlier interval 1300-1600 UT with magnetic enhancements #1- #3.

2.6. Global ground-based magnetic variations

The global dynamics of geomagnetic field perturbations was studied using 1-min magnetic data provided by an INTERMAGNET of ground magnetometers (http://www.intermagnet.org/index-eng.php). Since there were no pressure pulses in the upstream solar wind and auroral activity was low (see Figure 3), we expect that variations in the geomagnetic field (if any) should result from the local magnetosheath pressure pulses. We used magnetic stations located at geomagnetic latitudes below ~60° (Table 3), where a significant effect of different propagation time of magnetohydrodynamic (MHD) waves in the magnetosphere will be almost hidden at 1 min resolution. We grouped magnetic stations in meridional and latitudinal chains.

Figure 9 presents relative variations of horizontal (H) component, which was measured at equatorial and low latitudes ranging from 0° to ~20° of geomagnetic latitude in the interval from 1100 to 1600 UT. In Figure 9, the stations are arranged in local time from morning to postmidnight. The THEMIS magnetic field measurements are also shown at bottom. Four magnetic field pulses of different amplitudes are seen around ~1200, ~1335-1345, ~1422-1430 and ~1545-1550 UT practically at all stations. The last three pulses correspond to those observed by THEMIS at ~1334, ~1421 and 1547-1550 UT (#1 - #3, see also Table 2). Moreover, one can see the same pattern of magnetic variation "enhancement and decrease" in both ground-based and satellite observations. Note that the first magnetic pulse at ~1200 UT can not be emerged from THEMIS data because of the large background magnetic field in the inner magnetosphere. Magnetic records at daytime and nighttime are clearly distinguished by amplitudes and time delay relatively to the THEMIS data.

Magnetic records at nighttime stations (PHU, GZH, KNY, KDU, GUA, HON, PPT) are characterized by prominent variations of H component, with peak-to peak amplitudes of 3 - 5 nT. The dayside stations (KOU, VSS, MBO, ASC, TSU, BNG, AAE, ABG) show relative weak, but still distinguished, magnetic humps. Smaller amplitude at daytime is a result of an amplifying integral effect from the Chapman-Ferraro current at the magnetopause and ionospheric Sq-current at the ground.

It is interesting, that the magnetic pulse at 1200 UT is simultaneously (within the accuracy of ~1 min resolution) observed in all local time sectors. However, the other three enhancements were observed in different LT sectors at slightly different time. A time difference varies from ~2 min to ~10 min. The time delay depends on the time moment when a jet interacts with the magnetopause in a given latitude-longitude sector (Dmitriev and Suvorova, 2012).

We draw attention to the fact that low-latitude HON and PPT stations, which were located in the predawn sector (2-5 LT) from 1300 to 1500 UT, demonstrate the best coincidence (with a delay of ~1 min) of magnetic enhancements #1 and #2 with those observed by THEMIS near noon. Nighttime and daytime stations (PHU, GZH, KNY, KDU, GUA, MBO, ASC, TSU, BNG, AAE, ABG) observed these peaks with ~3 - 5 min delay. The longest delay (~7 min) for pulses #1 and #2 is found at morning/prenoon stations KOU and VSS (~9 - 11 LT).

As we have showed above, the FEE injections (F1 - F6 in Table 1) occur from ~2 to 5 LT. So, we present meridional chains of stations in the predawn and midnight sectors (Figure 10). All magnetic enhancements are well recognized from 0° to 60° of geomagnetic latitude. In midnight and predawn sectors, the first magnetic pulse at ~1200 UT was observed practically simultaneously everywhere. Magnetic pulse #1 around ~1333 UT was delayed by ~7 min at midlatitudes (30°-60°) in the midnight sector (left panel) and by ~5 min in the predawn sector (right panel). The pulse #2 shows a smaller delay (~3 min) at midlatitudes. The magnetic pulse #3 at most stations in both sectors is observed around ~1545 UT, that is 2 min earlier than at TH-E and 1 min later than at GOES (see Table 2). Thus, the low and middle latitude geomagnetic observations in all local time sectors demonstrate that the magnetic variations of "enhancement-decrease" pattern at 1200-1600 UT were observed by ground magnetometers as a global phenomenon.

3. Discussion and Summary

In this work, using NOAA/POES and THEMIS satellites we investigated an unusual case of deep injections of >30 keV electrons at L< 1.2 and associated FEE enhancements occurred during quiet, nonstorm condition on August 1, 2008. A series of postmidnight/predawn injections of >30 keV electrons could be associated with transient magnetospheric magnetic field perturbations. These magnetic perturbations were observed globally like "compression-expansion" effects by THEMIS and GOES 12 in the magnetosphere and by most of ground-based magnetometers from INTERMAGNET network. Comparative analysis of the THEMIS, OMNI and ACE data showed that the magnetic perturbations were caused by impact on the magnetopause by a series of plasma pressure pulses, so-called jets, propagated through the magnetosheath but not in the undisturbed upstream solar wind. Such plasma jets are typical consequence of the foreshock dynamics driven by variations in the IMF orientation (e.g., Lin et al., 1996) and are comprehensively studied using THEMIS and MMS missions (e.g., Archer et al., 2012; 2013; Dmitriev and Suvorova, 2012; 2015; Plaschke et al., 2017). For our case, THEMIS measurements in the region in front of the bow shock, showed obvious evidences of transient quasi-parallel bow shock and foreshock conditions during the interval.

The strong FEE enhancements with intensity of up to ~10^5 (cm^2 s sr)$^{-1}$ were observed by POES above central and eastern Pacific for a long time from ~1300 to 2300 UT. With analysis of longitudinal and local time distributions of the enhancements we identified a series of nightside injections occurred in the sector of 2 - 5 LT during the period from ~1300 to ~1700 UT (Figure 2). We found that the first 6 injections (Table 1) occurred before intensification of auroral activity at 1600 - 1800 UT, and hence, cannot be related to the substorm. Two injections occurred during the interval of weak auroral activity.

The quiet geomagnetic conditions in the period of 1300 - 1600 UT are consistent with undisturbed solar wind conditions, which can be obtained from the OMNI data and ACE upstream monitor. However, the picture, emerged from the THEMIS-C magnetic observations right upstream of the subsolar bow shock, showed an apparent discrepancy with OMNI in the magnetic field structures (see Figure 5). For our case, the discrepancy appeared to be due to an inability to predict accurately the evolution of small-scaled structures (e.g, Zastenker et al., 2000; Borovsky, 2008), especially with quasi-radial magnetic tubes, during the propagation to the Earth, and, as result, a notable uncertainty in the time lag method applied in the OMNI database. Erroneous time lag is typical for cases of the quasi-radial IMF orientation (e.g., Case and Wild, 2012; Mailyan et al., 2008; McPherron et al., 2013; Bier et al., 2014; Suvorova and Dmitriev, 2016). At worst, THEMIS-C observed magnetic field structures different from those in OMNI (as example see Figure 5). The actual solar wind parameters affecting the magnetosphere were related to a subsolar foreshock. The analysis of the THEMIS observations helps us to recognize possible external drivers, which might be responsible for the deep FEE injections.

During the period 1200 - 1800 UT, the magnetosphere was periodically under the quasi-radial IMF conditions (Figure 5). During that time, THEMIS-C observed intense ULF activity in the foreshock region. It is well known that the foreshock is also accompanied by ULF waves observed inside the magnetosphere by satellites and ground based magnetometers (e.g., Guglielmi, 1974; Clausen et al., 2009; Bier et al., 2014). We study the geomagnetic response with using THEMIS (D, E), GOES-12 geosynchronous satellite, and INTERMAGNET network of ground-base magnetometers. We find that the magnetospheric ULF waves are not strong enough to produce anomalous radial transport of energetic electrons at $L < 1.2$.

The THEMIS and GOES measurements clearly show several local effects of magnetosphere compression and expansion in the interval 1200 - 1600 UT (#1 - #3 in Table 2). Similar signatures were found in the H component at majority of ground stations (Figures 9 and 10). Though the geomagnetic response was global, the magnetic pulses were observed first at low latitudes in the postmidnight/predawn sector (2-5 LT). The amplitude of geomagnetic pulses is not very high: from few nT at ground to a few tens of nT at THEMIS. It should be noted that such magnetic perturbations are too weak to produce deep injections of >30 keV electrons below the radiation belt.

Analysis of the later interval 1600 - 1800 UT (Figure 7) indicated a possible cause of the magnetic variations (peaks #4 - #10 in Table 2). During that time, THEMIS (D, E) observed magnetic pulses, some of which were accompanied by penetrations of magnetosheath plasma into the magnetosphere. THEMIS also encountered the magnetosheath for a few minutes. We have found that the properties of magnetosheath plasma structures correspond well to high-speed plasma jets [Dmitriev and Suvorova et al., 2012]. The interaction of jets with the magnetopause results in geomagnetic pulses and penetration of the magnetosheath plasma inside the magnetosphere (Figure 8).

Note that the upstream conditions observed by THEMIS-C during both time intervals (from 12 to 16 UT and from 16 to 18 UT) were similar in that the quasi-radial IMF appeared. Hence, it is reasonable to suggest that the geomagnetic pulses occurred from 12 to 16 UT were also produced by jets because there were no strong enhancements in the solar wind dynamic pressure *P*d. Indeed, as one can see in Figures 3 and 8, tenuous variations of *P*d do not exceed a few tenths of nPa and, thus, they cannot produce sharp geomagnetic pulses with amplitudes of ~10 nT.

The magnetosheath pressure pulses or plasma jets arose during time intervals when quasi-radial IMF tubes were passing the subsolar bow shock region as observed by THEMIS. The foreshock was occasionally moving in or out of the subsolar region (see Figure 5). As the spacecraft crossed an interface between two flux tubes, it observed a rotation discontinuity. Passages of the rotational discontinuities followed by change between quasi-parallel and quasi-perpendicular bow shock regimes created favorable conditions for generation of plasma jets (Lin et al., 1996). Note that jets can be generated by directional discontinuities in absence of foreshock conditions (cases #1 and #5) (Dmitriev and Suvorova 2012). THEMIS was able to observe directly such plasma jets in the magnetosheath at later time, when it approached closely the magnetopause. Similar effects of transient magnetospheric compression and expansion and their signatures at low-latitudinal ground magnetometers were studied by Dmitriev and Suvorova (2012, 2015). As they established, such magnetic field perturbations were caused by magnetosheath plasma jets striking the dayside magnetopause during a foreshock transition through the subsolar region toward flank.

Another important effect is penetration of the magnetosheath plasma into the dayside magnetosphere due to interaction of large-scale jets with the magnetopause (Dmitriev and Suvorova, 2015). Recently, it was revealed that the magnetosheath high-speed jets result in auroral brightening on the dayside (Han et al., 2017; Wang et al., 2018). Sometimes, the dayside aurora penetrates to lower geomagnetic latitudes of ~72º from the discrete aurora oval at geomagnetic latitude ~76º, so-called throat aurora. Han et al. (2017) found that quasi-radial IMF or subsolar foreshock condition is favorable for occurrence of dayside throat aurora, whereas southward IMF has a weaker influence on its occurrence. Based on the comprehensive study of properties of throat aurora, Han et al. (2018) concluded that throat auroras are definite ground signatures for local magnetopause deformations and compressions produced by magnetosheath plasma jet impact. Han et al. (2016) provided direct evidence that the source of precipitating particles in the throat auroras was the magnetosheath plasma (sometimes mixed with magnetospheric plasma), which can be effectively transported by jets from the magnetosheath (e.g., Han et al., 2018). Thus, the jet impact is responsible for generating throat aurora, which provides enhancements in auroral ionospheric conductivity on the dayside.

The energy fluxes of hot plasma (from 50 eV to 10 keV) are measured by POES/TED plasma spectrometer. We conducted an additional analysis of hot plasma precipitations in the auroral region at *L*-shells from 7 to 15 during time interval from 11 to 18 UT on 1 August 2008. Figure 11 demonstrates magnetic observations by THEMIS-D and GOES-12, the energy fluxes of auroral precipitations, and FEE injections. We consider intense precipitations with the threshold of 0.5 (erg cm^{-2} s^{-1}), which is several times higher than the background. One can see that from 11 to 16 UT, the hot plasma precipitates mainly on the dayside (12 – 16 LT) while after 16 UT, the precipitations occur practically at all local times both on the day and night sides.

The first FEE injection (F1) at ~1250 UT was preceded by several geomagnetic pulses observed by GOES-12. The pulses were not very prominent because at that time, GOES-12 was located in the morning sector. One can see that some of pulses were accompanied by dayside auroral precipitations of the hot plasma. Note that POES satellites have 100 min orbital period and, hence, they can miss some of localized precipitations. On the other hand, when a jet hits the magnetopause, the magnetosheath plasma is not necessarily penetrating into the dayside magnetosphere and, hence, precipitating at high latitudes [*Dmitriev and Suvorova*, 2015]. Nevertheless, in Figure 11, we find two cases of geomagnetic pulses followed by intense dayside precipitations of the hot plasma at 1105 UT and 1144 UT.

Energetic electrons take a certain time dT to drift from the inner radiation belt edge (at L-shell L_1 = 1.2) to the heights of ~900 km (L-shell L_2 = 1.1~1.15):

$$dT(s) = 6380 * (L_1 - L_2)/V_{DE} \qquad (1)$$

where the ExB drift velocity is determined as

$$V_{DE} = 0.032 * L^3 * E, \qquad (2)$$

where L the average L-shell in the first approach and *E* is azimuthal electric field in mV/m. From equations (1) and (2), we estimate that the earthward drift of energetic electron across the magnetic field lines from *L* = 1.2 to *L* = 1.1 takes up to 40 min under local electric field of ~5 mV/m. Note that *E* ~ 5 mV/m was obtained in simulations of energetic electron injections at L < 1.3 [*Selesnick et al.*, 2016].

In our case of non-storm conditions, it is hard to imagine that the strong azimuthal *E* can persist for so long time. Previously, simulations by Su et al. (2016) have showed that it is not necessary for electrons to be transported earthward all the way during a single injection. Hence, we can consider a multi-step radial transport produced by a number of short pulses of *E*. In this case, the drift from L=1.2 to L=1.1 requires two or more pulses of ~10 min duration that is comparable with the duration of jet-related disturbances. The multi-step process is limited by the time, during which a particle stays in the region of injection. The >30 keV electrons have a long period of azimuthal drift and, thus, they can stay in the region for hours. In contrast, the >100 keV electrons with the azimuthal period of ~6 h leave quickly the injection region and, thus, do not have enough time to penetrate to the forbidden zone. This effect can explain the absence of high-energy electrons in the FEE enhancements presented.

We can suggest that the first FEE injection required a long time (~hour and longer) and several pulses of *E* in order to transport energetic electrons from undisturbed edge of the inner radiation belt to L~1.1. Then, >30 keV electrons populate L-shells from 1.15 to 1.1 that makes possible to transport electrons to 900 km heights for a short time of ~10 min by one pulse of strong *E*. The latter pattern is applicable for the FEE injection F2 and others. As one can see in Figure 11, each FEE injection after 13 UT is preceded within <30 min by intense auroral precipitations of the hot plasma. The latter is accompanied with geomagnetic pulses produced by the interaction of jets with the magnetopause. It is important to remind that tenuous variations of the solar wind dynamic pressure could not produce the geomagnetic perturbations occurred during the interval considered.

We associate the dayside precipitations at high latitudes with the effect of jets piercing the magnetopause. The jets provide penetration of hot plasma from the magnetosheath to the magnetosphere. Dmitriev and Suvorova (2015) have found that the average rate of jet-related penetration of the magnetosheath plasma into the magnetosphere is about 10^{29} particles per day. The penetrated hot ions move quickly (within a few minutes) along the magnetic field lines to high-latitude regions of the dayside ionosphere. We can estimate the flux of precipitating ions of ~10^7 to 10^8 (cm^2 s)$^{-1}$ if we assume that particles precipitate on the dayside arc of 3º width at 70º latitude. This particle flux corresponds well to the energy fluxes of precipitating ions (>0.5 erg cm^{-2} s^{-1}) measured by POES/TED at high latitudes (see Figure 11). Hence, the jet-related magnetosheath plasma can produce significant additional ionization and increase conductivity of the high-latitude ionosphere on the dayside. An enhancement of electric currents in the dayside ionosphere should induce an enhancement of the electric field on the nightside and especially in the predawn sector, where the conductivity is weak. The nightside electric field might penetrate from high to low latitudes and produce ExB drift of electrons from the inner radiation belt to lower heights.

Thus, we can propose a scenario when magnetosheath plasma jets, associated with dynamical subsolar foreshock and rotational discontinuities, interact with the dayside magnetopause and cause compression effect with magnetic field perturbations and effective transport of the magnetosheath plasma inside the magnetosphere. The magnetosheath plasma or mix with magnetospheric plasma precipitates to the dayside ionosphere at high latitudes that result in a local increase of the ionospheric conductivity. This in turn promotes generation of transient localized electric fields, which are able to penetrate from high latitudes to very low latitudes (low L-shells). Most favorable conditions for penetration of localized electric fields and FEE enhancements arise in the period from May to September independently on geomagnetic activity level (Suvorova, 2017). Our case event on 1 August 2008 corresponds well to these favorable conditions.

Anomalous transport and loss of energetic particles in the magnetosphere was studied and modeled in numerous papers (e.g., Glocer et al., 2011; Selesnick et al., 2016; Su et al., 2016; Turner et al., 2015; Turner et al., 2017a; Zhao and Li, 2013; Zhao et al., 2017a). In the present case, the magnetosphere is driven rather by plasma jets generated locally in the magnetosheath. Moreover, we show that the solar wind conditions right upstream of the bow shock can be substantially different from those measured in the far upstream regions. Another serious problem is the generation/penetration of electric fields in the inner magnetosphere, which is far from complete understanding. Numerical estimations show that the anomalous (fast) radial transport of particles observed in the inner magnetosphere can be produced by the electric field up to 5 mV/m (Selesnick et al., 2016; Suvorova et al., 2013). At the present time, there are no models predicting strong electric fields in the inner radiation belt and below. In this sense the scenarios suggested here requires further development of new advanced models of the magnetosheath – magnetosphere – ionosphere coupling.

Acknowledgements

The authors thanks a team of NOAA’s Polar Orbiting Environmental Satellites for providing experimental data about energetic particles, the CDAWEB for providing the ACE solar wind data and Kyoto World Data Center for Geomagnetism (http://wdc.kugi.kyoto-u.ac.jp/index.html) for providing the geomagnetic indices. We thank the THEMIS team for magnetic and plasma data provided. The results presented in this paper rely on data collected at magnetic observatories. We thank the national institutes that support them and INTERMAGNET for promoting high standards of magnetic observatory practice (www.intermagnet.org). The OMNI data are provided by the GSFC/SPDF OMNIWeb platform (http://cdaweb.gsfc.nasa.gov/). The work was supported by grant MOST 106-2811-M-008-050 and MOST 106-2111-M-008-030-MY3 to National Central University.

References

Archer, M. O., Horbury, T. S., and Eastwood, J. P.: Magnetosheath pressure pulses: Generation downstream of the bow shock from solar wind discontinuities, J. Geophys. Res., 117, A05228, https://doi.org/10.1029/2011JA017468, 2012.

Archer, M. O., Horbury, T. S., Eastwood, J. P., Weygand, J. M., and Yeoman, T. K.: Magnetospheric response to magnetosheath pressure pulses: A low-pass filter effect, J. Geophys. Res., 118, 5454-5466, https://doi.org/10.1002/jgra.50519, 2013.

Asikainen, T., and Mursula, K.: Filling the South Atlantic anomaly by energetic electrons during a great magnetic storm, Geophys. Res. Lett., 32, L16102, https://doi.org/10.1029/2005GL023634, 2005.

Auster, H. U., Glassmeier, K. H., Magnes,W., Aydogar, O., Baumjohann, W., Constantinescu, D., Fischer, D., Fornacon, K. H., Georgescu, E., Harvey, P., Hillenmaier, O., Kroth, R., Ludlam, M., Narita, Y., Nakamura, R., Okrafka, K., Plaschke, F., Richter, I., Schwarzl, H., Stoll, B., Valavanoglou, A., Wiedemann, M.: The THEMIS fluxgate magnetometer, Space Sci. Rev., 141(1–4), 235– 264, https://doi.org/10.1007/s11214-008-9365-9, 2008.

Bier, E. A., Owusu, N., Engebretson, M. J., Posch, J. L., Lessard, M. R., and Pilipenko V. A.: Investigating the IMF cone angle control of Pc3-4 pulsations observed on the ground, J. Geophys. Res. Space Physics, 119, 1797-1813, https://doi.org/10.1002/2013JA019637, 2014.

Borovsky, J. E.: Flux tube texture of the solar wind: Strands of the magnetic carpet at 1 AU? J. Geophys. Res., 113, A08110, https://doi.org/10.1029/2007JA012684, 2008.

Case, N. A., and Wild, J. A.: A statistical comparison of solar wind propagation delays derived from multispacecraft techniques, J. Geophys. Res., 117, A02101, https://doi.org/10.1029/2011JA016946, 2012.

Clausen, L. B. N., Yeoman, T. K., Fear, R. C., Behlke, R., Lucek, E. A., and Engebretson, M. J.: First simultaneous measurements of waves generated at the bow shock in the solar wind, the magnetosphere and on the ground, Annales Geophysicae, 27, 357-371, https://doi.org/10.5194/angeo-27-357-2009, 2009.

Crooker, N. U., Eastman, T. E., Frank, L. A., Smith, E. J., and Russell, C. T.: Energetic magnetosheath ions and the interplanetary magnetic field orientation, J. Geophys. Res., 86, 4455-4460, 1981.

Dmitriev, A. V., and Suvorova, A. V.: Traveling magnetopause distortion related to a large-scale magnetosheath plasma jet: THEMIS and ground-based observations, J. Geophys. Res., 117, A08217, https://doi.org/10.1029/2011JA016861, 2012.

Dmitriev, A. V., and Suvorova, A. V.: Large-scale jets in the magnetosheath and plasma penetration across the magnetopause: THEMIS observations, J. Geophys. Res. Space Physics, 120, 4423–4437, https://doi.org/10.1002/ 2014JA020953, 2015.

Dmitriev, A. V., and Yeh, H.-C.: Storm-time ionization enhancements at the topside low-latitude ionosphere, Ann. Geophys., 26, 867-876, 2008.

Dmitriev, A. V., Suvorova, A.V., Klimenko, M. V., Klimenko, V. V., Ratovsky, K. G., Rakhmatulin, R. A., and Parkhomov, V. A.: Predictable and unpredictable ionospheric disturbances during St. Patrick's Day magnetic storms of 2013 and 2015 and on 8-9 March 2008, J. Geophys. Res.: Space Physics, 122, 2398-2432, https://doi.org/10.1002/2016JA023260, (2017).

Glocer, A., Fok, M.-C., Nagai, T., Tóth, G., Guild, T., and Blake, J.: Rapid rebuilding of the outer radiation belt, J. Geophys. Res., 116, A09213, https://doi.org/10.1029/2011JA016516, 2011.

Gosling, J. T., Asbridge, J. R., Bame, S. J., Paschmann, G., and Sckopke, N.: Observations of two distinct populations of bow shock ions in the upstream solar wind, J. Geophys. Res., 5, 957–960, 1978.

Greenstadt, E. W., Russell, C. T., and Hoppe, M.: Magnetic field orientation and suprathermal ion streams in the earth’s foreshock, J. Geophys. Res., 85, 3473–3479, 1980.

Guglielmi, A.: Diagnostics of the magnetosphere and interplanetary medium by means of pulsations, Space Sci. Rev., 16(3), 331–345, 1974.

Evans, D. S.: Dramatic increases in the flux of >30 keV electrons at very low L-values in the onset of large geomagnetic storms, EOS Trans., 69(44), 1393, 1988.

Evans, D. S., and Greer, M. S.: Polar Orbiting Environmental Satellite Space Environment Monitor: 2. Instrument descriptions and archive data documentation. Tech. Memo. version 1.4, NOAA Space Environ. Lab., Boulder, Colo., 2004.

Heikkila, W. J.: Soft particle fluxes near the equator, J. Geophys. Res., 76, 1076-1078, 1971.

Han, D.-S., Nishimura, Y., Lyons, L. R., Hu, H.Q., and Yang, H. G.: Throat aurora: The ionospheric signature of magnetosheath particles penetrating into the magnetosphere, Geophysical Research Letters, 43, 1819-1827, https://doi.org/10.1002/2016GL068181, 2016.

Han, D.-S., Hietala, H., Chen, X.-C., Nishimura, Y., Lyons R. L., Liu, J.-J., Hu, H.-Q., and Yang, H.-G.: Observational properties of dayside throat aurora and implications on the possible generation mechanisms, J. Geophys. Res. Space Physics, 122, 1853-1870, https://doi.org/10.1002/2016JA023394, 2017a.

Han, D.-S., Liu, J.-J., Chen, X.-C., Xu, T., Li, B., Hu, Z.-J., Hu, H. Q., Yang, H. G., Fuselier, S. A., and Pollock, C.J.: Direct evidence for throat aurora being the ionospheric signature of magnetopause transient and reflecting localized magnetopause indentations. J. Geophys. Res. Space Physics, 123, 2658-2667, https://doi.org/10.1002/2017JA024945, 2018.

Imhof, W. L., Gaines, E. E., and Reagan, J. B.: Dynamic variations in intensity and energy spectra of electrons in the inner radiation belt. J. Geophys. Res., 78(22), 4568–4577, 1973a.

Kikuchi, T. and Evans, D.S.: Energetic electrons observed by NOAA-6 over Japan (L=1.3) at the time of geomagnetic storm on February 8-9, 1986, Proc. Res. Inst. Atmos., Nagoya University, 36, 137-150, 1989.

King, J. H., and Papitashvili, N. E.: Solar wind spatial scales in and comparisons of hourly Wind and ACE plasma and magnetic field data, J. Geophys. Res., 110, A02104, https://doi.org/10.1029/2004JA010649, 2005.

Krasovskii, V. I., Shklovski, I. S., Galperin, Yu. I., Svetlitskii, E. M., Kushnir, Yu. M., and Bordovskii, G. A.: The detection of electrons with energies of approximately l0 keV in the upper atmosphere (in Russian). Iskusstvennye Sputniki Zemli, 6, 113-126, (English translation: Planet. Space Sci., 9, 27-40, 1962), 1961.

Lejosne, S., and Mozer, F. S.: Typical values of the electric drift E × B/B2 in the inner radiation belt and slot region as determined from Van Allen Probe measurements, J. Geophys. Res. Space Physics, 121, 12,014–12,024, https://doi.org/10.1002/2016JA023613, 2016.

Lin, Y., Lee, L. C., and Yan, M.: Generation of dynamic pressure pulses downstream of the bow shock by variations in the interplanetary magnetic field orientation, J. Geophys. Res., 101, 479–493, 1996.

Lin, R. L., Zhang, X. X. , Liu, S. Q., Wang, Y. L., and Gong, J. C.: A three-dimensional asymmetric magnetopause model. J. Geophys. Res., 115, A04207, https://doi.org/10.1029/2009JA014235, 2010.

Mailyan, B., Munteanu, C., and Haaland, S.: What is the best method to calculate the solar wind propagation delay? Ann. Geophys., 26, 2383–2394, 2008.

Matsui, H., Torbert, R. B., Spence, H. E., Khotyaintsev, Yu. V., and Lindqvist, P.-A.: Revision of empirical electric field modeling in the inner magnetosphere using Cluster data, J. Geophys. Res. Space Physics, 118, 4119–4134, https://doi.org/10.1002/jgra.50373, 2013.

McFadden, J. P., Carlson, C. W., Larson, D., Ludlam, M., Abiad, R., Elliott, B., Turin, P., Marckwordt, M., and Angelopoulos,V.: The THEMIS ESA plasma instrument and in-flight calibration, Space Sci. Rev., 141, 277–302, https://doi.org/10.1007/s11214-008-9440-2, 2008.

McIlwain, C. E.: Coordinates for mapping the distribution of magnetically trapped particles, J. Geophys. Res., 66, 3681-3691, 1961.

McPherron, R. L., Baker, D. N., Pulkkinen, T. I, Hsu,T. S., Kissinger, J., and Chu, X.: Changes in solar wind–magnetosphere coupling with solar cycle, season, and time relative to stream interface, J. Atmos. Sol. Terr. Phys., 99, 1-13, https://doi.org/10.1016/j.jastp.2012.09.003, 2013.

Park J., Min, K. W., Summers, D., Hwang, J., Kim, H. J., Horne, R. B., Kirsch, P., Yumoto, K., Uozumi, T., Lühr, H., and Green, J.: Non-stormtime injection of energetic particles into the slot region between Earth's inner and outer electron radiation belts as observed by STSAT-1 and NOAA-POES, Geophys. Res. Lett., 37, L16102, https://doi.org/10.1029/2010GL043989, 2010.

Paschmann, G., Sckopke, N., Bame, N., Gosling, J.T., Russell, C.T., and Greenstadt, E.W.: Association of low-frequancy waves with suprathermal ions in the upstream solar wind, Geophys. Res. Lett., 6, 209-212, 1979.

Paulikas, G. A.: Precipitation of particles at low and middle latitudes, Rev. Geophys. Space Phys., 13(5), 709-734, 1975.

Pfitzer, K. A., and Winckler, J. R.: Experimental observation of a large addition to the electron inner radiation belt after a solar flare event, J. Geophys. Res., 73(17), 5792–5797, 1968.

Plaschke, F., Karlsson, T., Hietala, H., Archer, M., Voros, Z., Nakamura, R., Magnes, W., Baumjohann, W., Torbert, R. B., Russell, C. T., and Giles, B. L.: Magnetosheath high-speed jets: Internal structure and interaction with ambient plasma, Journal of Geophysical Research: Space Physics, 122, 10,157–10,175, 2017.

Rowland, D. E., and Wygant, J. R.: Dependence of the large-scale, inner magnetospheric electric field on geomagnetic activity, J. Geophys. Res., 103(A7), 14959-24964, 1998.

Reeves, G. D., Friedel, R. H. W., Larsen, B. A., Skoug, R. M., Funsten, H. O., Claudepierre, S. G., Fennell, J. F., Turner, D. L., Denton, M. H., Spence, H. E., Blake, J. B., and Baker, D.N.: Energy-dependent dynamics of keV to MeV electrons in the inner zone, outer zone, and slot regions, J. Geophys. Res., 121, 397-412, https://doi.org/10.1002/2015JA021569, 2016.

Savenko, I. A., Shavrin, P. I., and Pisarenko, N. F.: Soft particle radiation at an altitude of 320 km in the latitudes near the equator (in russian). Iskusstvennye Sputniki Zemli, 13, 75-80 (English translation: Planet. Space Sci., 11, 431-436, 1963), 1962.

Schwartz, S. J., and Burgess, D.: Quasi-parallel shocks: A patchwork of three-dimensional structures, Geophys. Res. Lett., 18, 373-376, 1991.

Selesnick, R. S., Su, Y.-J., and Blake, J. B.: Control of the innermost electron radiation belt by large-scale electric fields, J. Geophys. Res. Space Physics, 121, 8417–8427, https://doi.org/10.1002/2016JA022973, 2016.

Sibeck, D. G.: Plasma transfer processes at the magnetopause, Space Sci. Rev., 88, 207–283, https://doi.org/10.1023/a:1005255801425, 1999.

Su, Y-J, Selesnick, R. S., and Blake J. B.: Formation of the inner electron radiation belt by enhanced large-scale electric fields, J. Geophys. Res. Space Physics, 121, 8508–8522, https://doi.org/10.1002/2016JA022881, 2016.

Suvorova, A. V., and Dmitriev, A. V.: Radiation aspects of geomagnetic storm impact below the radiation belt, In V. P. Banks (Ed.), Cyclonic and Geomagnetic Storms: Predicting Factors, Formation and Environmental Impacts, (pp. 19-75), New York: NOVA Science Publishers, Inc., 2015.

Suvorova, A. V., and Dmitriev, A. V.: On magnetopause inflation under radial IMF, Adv. Space Res., 58, 249-256, 2016.

Suvorova, A. V., Dmitriev, A.V., and Tsai, L.-C.: On relation between mid-latitude ionospheric ionization and quasi-trapped energetic electrons during 15 December 2006 magnetic storm, Planet. Space Sci., 60, 363-369, https://doi.org/10.1016/j.pss.2011.11.001, 2012.

Suvorova, A. V., Dmitriev, A. V., Tsai, L.-C., Kunitsyn, V. E., Andreeva, E. S., Nesterov, I. A., and Lazutin, L. L.: TEC evidence for near-equatorial energy deposition by 30 keV electrons in the topside ionosphere, J. Geophys. Res., 118, 4672–4695, https://doi.org/10.1002/jgra.50439, 2013.

Suvorova, A. V., Huang, C.-M., Matsumoto, H., Dmitriev, A. V., Kunitsyn, V. E., Andreeva, E. S., Nesterov, I. A., and Tsai, L.-C.: Low-latitude ionospheric effects of energetic electrons during a recurrent magnetic storm, J. Geophys. Res. Space Physics, 119, 9283-9303, https://doi.org/10.1002/2014JA020349, 2014.

Suvorova, A. V., Huang, C.-M., Dmitriev, A. V., Kunitsyn, V. E., Andreeva, E. S., Nesterov, I. A., Klimenko, M. V., Klimenko, V. V., and Tumanova, Yu. S.: Effects of ionizing energetic electrons and plasma transport in the ionosphere during the initial phase of the December 2006 magnetic storm, J. Geophys Res.: Space Physics, 121, 5880-5896, https://doi.org/10.1002/2016JA022622, 2016.

Suvorova, A.V.: Flux enhancements of >30 keV electrons at low drift shells L <1.2 during last solar cycles, J. Geophys Res.: Space Physics, 122, 12274-12287, https://doi.org/10.1002/2017JA024556, 2017.

Tadokoro, H., Tsuchiya, F., Miyoshi, Y., Misawa, H., Morioka, A., and Evans, D. S.: Electron flux enhancement in the inner radiation belt during moderate magnetic storms, Ann. Geophys., 25, 1359-1364, 2007.

Tanaka, Y., Nishino, M., and Iwata, A.: Magnetic storm-related energetic electrons and magnetospheric electric fields penetrating into the low-latitude magnetosphere (L~1.5), Planet. Space Sci., 38(8), 1051-1059, 1990.

Troshichev, O. A., Andrezen, V. G., Vennerstrøm, S., and Friis-Christensen, E.: Magnetic activity in the polar cap – A new index, Planet. Space Sci., 36(11), 1095–1102, 1988.

Turner, D. L., Claudepierre, S. G., Fennell, J. F., O'Brien, T. P., Blake, J. B., Lemon, C., Gkioulidou, M., Takahashi, K., Reeves, G. D., Thaller, S., Breneman, A., Wygant, J. R., Li, W., Runov, A., and Angelopoulos, V.: Energetic electron injections deep into the inner magnetosphere associated with substorm activity, Geophys. Res. Lett., 42, 2079-2087, https://doi.org/10.1002/2015GL063225, 2015.

Turner, D. L., Fennell, J. F., Blake, J. B., Claudepierre, S. G., Clemmons, J. H., Jaynes, A. N., Leonard, T., Baker, D. N., et al.: Multipoint observations of energetic particles injections and substorm activity during a conjunction between Magnetospheric Multiscale (MMS) and Van Allen Probes, J. Geophys. Res. Space Physics, 122, 11481-11504, https://doi.org/10.1002/2017JA024554, 2017a.

Turner, D. L., O'Brien, T.P., Fennell, J.F., Claudepierre, S. G., Blake, J. B., Jaynes, A. N., Baker, D. N., Kanekal, S., Gkioulidou, M., Henderson, M. G., and Reeves, G. D.: Investigating the source of near-relativistics and relativistics electrons in Earth's inner radiation belt, J. Geophys. Res. Space Physics, 122, 695-710, https://doi.org/ 10.1002/2016JA023600, 2017b.

Zastenker, G .N., Dalin, P. A., Petrukovich, A. A., et al.: Solar wind structure dynamics by multipoint observations, Phys. Chem. Earth (C), 25 (1-2), 137-140, 2000.

Zhao, H., and Li, X.: Modeling energetic electron penetration into the slot region and inner radiation belt, J. Geophys. Res. Space Physics, 118, 6936-6945, https://doi.org/10.1002/2013JA019240, 2013.

Zhao, H., Li, X., Baker, D.N., Claudepierre, S.G., Fennell, J. F., Blake, J. B., Larsen, B. A., Skoug, R. M., Funsten, H. O., Friedel, R. H. W., Reeves, G. D., Spence, H. E., Mitchell, D. G., and Lanzerotti, L. J.: Ring current electron dynamics during geomagnetic storms based on the Van Allen Probes measurements, J. Geophys. Res. Space Physics, 121, 3333-3346, https://doi.org/10.1002/2016JA022358, 2016.

Zhao, H., Baker, D.N., Califf, S., Li, X., Jaynes, A. N., Leonard, T., Kanekal, S. G., Blake, J. B., Fennell, J. F., Claudepierre, S. G., Turner, D. L., Reeves, G. D., and Spence, H. E.: Van Allen Probes measurements of energetic particle deep penetration into the low L region (L<4) during the storm on 8 April 2016, J. Geophys. Res., 122, 12140-12152, https://doi.org/10.1002/2017JA024558, 2017a.

Zhao, H., Baker, D. N., Jaynes, A. N., Li, X., Elkington, S. R., Kanekal, S. G., Spence, H. E., Boyd, A. J., Huang, C.-L., and Forsyth, C.: On the relation between radiation belt electrons and solar wind parameters/geomagnetic indices: Dependence on the first adiabatic invariant and L*, J. Geophys. Res. Space Physics, 122, 1624-1642, https://doi.org/10.1002/2016JA023658, 2017b.

Wang, B., Nishimura, Y., Heitala, H., Lyons, L., Angelopoulos, V., Plaschke,F., Ebihara,Y., and Weatherwax, A.: Impacts of magnetosheath high-speed jets on the magnetosphere and ionosphere measured by optical imaging and satellite observations, J. Geophys. Res. Space Physics, 123, 4879-4894, https://doi.org/10.1002/2017JA024954, 2018.

Table 1 *FEE Enhancements observed by POES satellites*

FEE ID #	POES s/c ID	Observed time hh:mm UT	Longitude deg	LT* h
F1	P8	12:50	-164.2	1.8
F2	P5	13:15	-128.8	5.1
F3	P6	13:53	-138.3	5.1
F4	P8	14:32	169.7	1.6
F5	P5	14:54	-152.7	5.1
F6	P6	15:34	-162.5	5.0
F7	P2	15:44	-98.7	9.3
F8	P5	16:33	-170.1	5.0
F9	P7	16:37	-107.3	9.7
F10	P6	17:12	180.0	4.9
F11	P2	17:24	-123.0	9.4
F12	P7	18:16	-131.0	9.8
F13	P2	19:06	-140.0	9.6
F14	P8	20:30	-105.0	13.8
F15	P6	23:09	-94.5	17.2

* Local time

Table 2 *Timing of Magnetic Field Enhancements and Plasma Pulses from THEMIS and GOES12*

ID #	s/c ID	Time of magnetic peak hh:mm:ss	Time of pressure pulse hh:mm:ss	Foreshock signatures
1	TH-D	13:33:40		absent
	TH-E	13:33:40		
	TH-B	13:33:40		
	G12	13:35:40		
2	TH-D	14:20:50		ions, ULF
	TH-E	14:20:50		
	TH-B	14:20:50		
	G12	14:20:50		
3	TH-D	15:50:30		ions, ULF
	TH-E	15:47:30		
	G12	15:44:00		
4	TH-D	16:14:05	~16:15 - 16:16	ions, ULF
	TH-E	16:14:05		
5	TH-D	16:38:20	16:40	absent
	TH-E	16:38:40		
6	TH-D	16:47:45	16:47:55	ions
	TH-E	16:47:45		
7	TH-D	-	16:51:22	ions, ULF
	TH-E	-		
8	TH-D	magnetosheath	17:00:25	ions, ULF
	TH-E	-		
9	TH-D	magnetosheath	~17:12 - 17:13	ions
	TH-E	17:12:30		
10	TH-D	17:24:50	17:24:50	ions, ULF
	TH-E	-		

Table 3

Location of Magnetic Stations in Geographic and Geomagnetic coordinates

Code	Name	GLat[a]	GLon[a]	MLat[b]	MLon[b]
AAE	Addis Ababa	9.0	38.8	5.3	109.9
ABG	Alibag	18.6	72.9	9.5	144.4
ASC	Ascension Island	-8.0	-14.4	-1.4	54.7
ASP	Alice Springs	-23.8	133.9	-34.1	-153.6
BNG	Bangui	4.3	18.6	4.6	89.3
CMO	College	64.9	-147.9	64.8	-102.6
CNB	Canberra	-35.3	149.4	-43.8	-134.5
CTA	Charters Towers	-20.1	146.3	-29.1	-140.7
EYR	Eyrewell	-43.4	172.4	-47.8	-107.0
GUA	Guam	13.6	144.9	4.2	-146.3
GZH	Zhaoqing	23.0	112.5	11.7	-177.1
HON	Honolulu	21.3	-158.0	21.2	-92.7
KAK	Kakioka	36.2	140.2	26.2	-153.3
KDU	Kakadu	-12.7	132.5	-23.2	-156.3
KNY	Kanoya	31.4	130.9	20.7	-161.2
KOU	Kourou	5.2	-52.7	16.1	17.7
MBO	Mbour	14.4	-17.0	21.1	55.8
MCQ	McQuarie Island	-54.5	159.0	-60.9	-116.2
MMB	Memambetsu	43.9	144.2	34.2	-150.9
PET	Paratunka	53.0	158.3	45.6	-138.5
PHU	Phuthuy	21.0	106.0	9.7	176.0
PPT	Pamatai	-17.6	-149.6	-15.2	-76.5
SHU	Shumagin	55.4	199.5	54.1	-103.1
SIT	Sitka	57.1	-135.3	60.1	-83.7
TSU	Tsumeb	-19.2	17.6	-18.3	83.5
VSS	Vassouras	-22.4	-43.7	-12.1	24.6

[a] Geographic latitude and longitude

[b] Magnetic latitude and longitude

FIGURE CAPTIONS

Figure 1. Geographic distribution of >30 keV electron fluxes measured by five NOAA/POES satellites on August 1, 2008 for the time interval (a) 0-12 UT, before the electron flux enhancements and (b) 12-24 UT, during the enhancements. The electrons are detected in vertical direction. In the forbidden zone those electrons are quasi-trapped. The electron fluxes enhanced largely during nonstorm condition after 12 UT. The forbidden zone is bounded by L=1.2 (white lines) and located outside of the South Atlantic Anomaly (SAA) at equatorial-to-low latitudes. The solid black curve indicates the dip equator.

Figure 2. FEE enhancements on 1 August 2008: (a) fluxes of >30 keV electrons in units $(cm^2\ s\ sr)^{-1}$, (b) L-shell of enhancements, (c) longitude and (d) local time of peak fluxes (black circles). Measurements within the SAA area are indicated by the open circles. Colorful curves denote NOAA/POES satellites: P2 (black), P5 (pink), P6 (red), P7 (blue), and P8 (green). Horizontal dashed line at panel (b) depicts the lower edge of the inner radiation belt. FEE enhancements peak at the equator (minimal L-shells) that indicates a fast radial transport from the inner radiation belt.

Figure 3. Solar wind parameters from OMNI data and geomagnetic indices on August 1, 2008. From top to bottom: (a) solar wind density (black) and dynamic pressure (blue), (b) solar wind speed, (c) interplanetary magnetic field (IMF) components Bx (blue), By (green), Bz (red) and magnitude B (black) in Geocentric Solar Magnetospheric (GMS) coordinates, (d) polar cap magnetic activity index PCN for northern (blue) and PCS for southern (red) hemispheres, (e) auroral electrojet index AE (black), AL (red), AU (green), and (f) storm time ring current variation index SYM-H. The shaded box denotes the time interval from 13 to 23 UT, when the nonstorm FEE enhancements were observed.

Figure 4. Spacecraft positions in GSM coordinates from 1200 to 1800 UT on August 1, 2018. The TH-C probe (blue) was in front of the subsolar bow shock. The TH-E (orange), TH-D (green), TH-B (brown), and GOES 12 (black) were located inside the dayside magnetosphere. The magnetopause position (black curve) was calculated using OMNI data for the upstream conditions at ~1600 UT following the model by Lin et al.'s (2010).

Figure 5. Observations of plasma and magnetic field on August 1, 2008. (a) Ion spectrogram (ion flux is in units of eV/cm^2 s sr eV) and IMF vector components in GSM coordinates measured by TH-C, (b) IMF vector components from OMNI data set, (c) IMF cone angles plotted for TH-C (red) and OMNI (black).

Figure 6. Satellite measurements of magnetic field and plasma in the dayside magnetosphere and geomagnetic activity. (a) The Bz-GSM components from THEMIS probes TH-B (brown), TH-E (orange), and TH-D (green). The left y-axis corresponds to the magnetic measurements from TH-B and TH-D, and the right y-axis to TH-E. (b) The magnetic field strength from GOES-12 (black); (c) the SYM-H index; and (d) the ion spectrogram from TH-D (ion flux is in units of eV/cm^2 s sr eV). Dashed lines, numbered from 1 to 10, indicate time moments of magnetic and plasma disturbances observed by THEMIS.

Figure 7. Observations of plasma and magnetic field at 1530-1800 UT on August 1, 2008: (a-c) ion spectrograms measured by TH-C, TH-D, and TH-E (ion flux is in units of eV/cm^2 s sr eV), (d) SYM-H index, (e) AE (black) and AL (red) indices, (f) horizontal magnetic field Hp detected by GOES 12 from 10 to 13 LT, (g) magnetic field strengths Btot from TH-D (green) and TH-E (red), (h) IMF cone angles for TH-C (black) and for the ACE upstream monitor (blue). The ACE measurements are delayed by 60 min. Dashed lines and numbers #4 - #10 mark magnetospheric disturbances with magnetosheath ion population observed in the magnetosphere.

Figure 8. Observations of plasma and magnetic field during the intervals 1600 - 1630 UT, 1630 - 1700 UT and 1658 - 1728 UT on August 1, 2008. Panels show from top to bottom: (a) ion spectrogram from TH-D, (b) total pressure Ptot measured by the ACE upstream monitor (black) and TH-D (red), (c) plasma density D measured by ACE (black) and TH-D (blue), (d) TH-D measurements of bulk velocity V (black) and its components in GSM coordinates Vx (blue), Vy (green) and Vz (red), (e) transversal components of magnetic field Bx (blue) and By (green) from TH-D, (f) magnitude B and Bz component of magnetic field from TH-D, (g) magnitude B and Bz component of magnetic field from TH-E. The magnetosheath plasma penetration is denoted by dashed lines and numbers #4 - #10.

Figure 9. Relative variations in the horizontal component (H) of the geomagnetic field at low geomagnetic latitudes. Local time intervals are indicated near the station codes. The vertical lines depict time of the magnetic pulses at THEMIS (lines #1 - #3). Bottom panel shows magnetic field B measured by TH-E (orange) and by TH-D (green).

Figure 10. Relative variations in the horizontal component (H) of the geomagnetic field in the midnight (left) and predawn (right) sectors. The geomagnetic latitudes of the stations are indicated near station codes. The vertical lines depict time of the magnetic pulses at THEMIS.

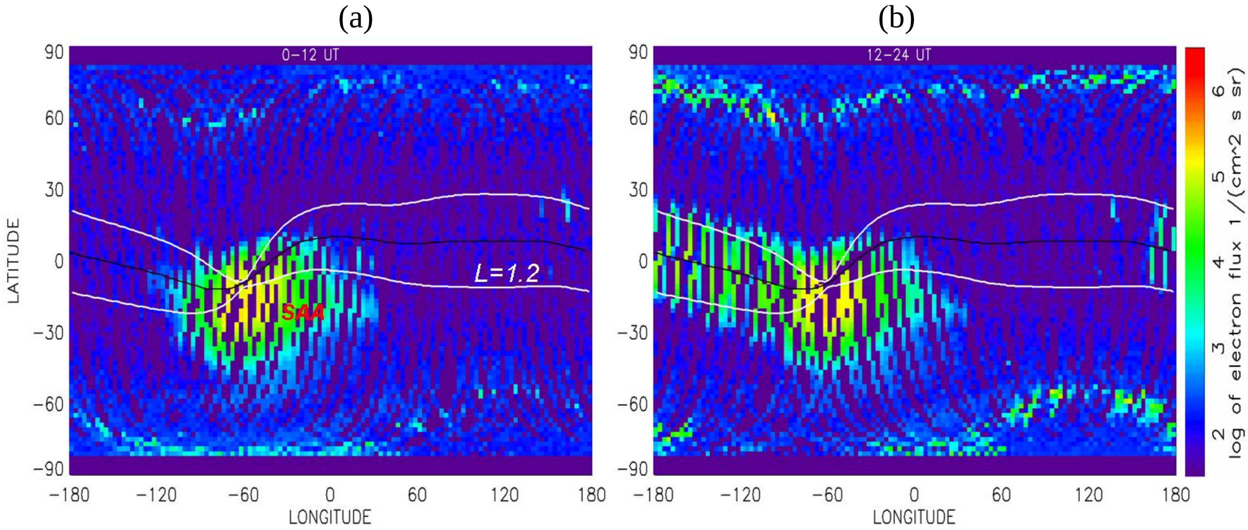

Figure 1. Geographic distribution of >30 keV electron fluxes measured by five NOAA/POES satellites on August 1, 2008 for the time interval (a) 0-12 UT, before the electron flux enhancements and (b) 12-24 UT, during the enhancements. The electrons are detected in vertical direction. In the forbidden zone those electrons are quasi-trapped. The electron fluxes enhanced largely during nonstorm condition after 12 UT. The forbidden zone is bounded by L=1.2 (white lines) and located outside of the South Atlantic Anomaly (SAA) at equatorial-to-low latitudes. The solid black curve indicates the dip equator.

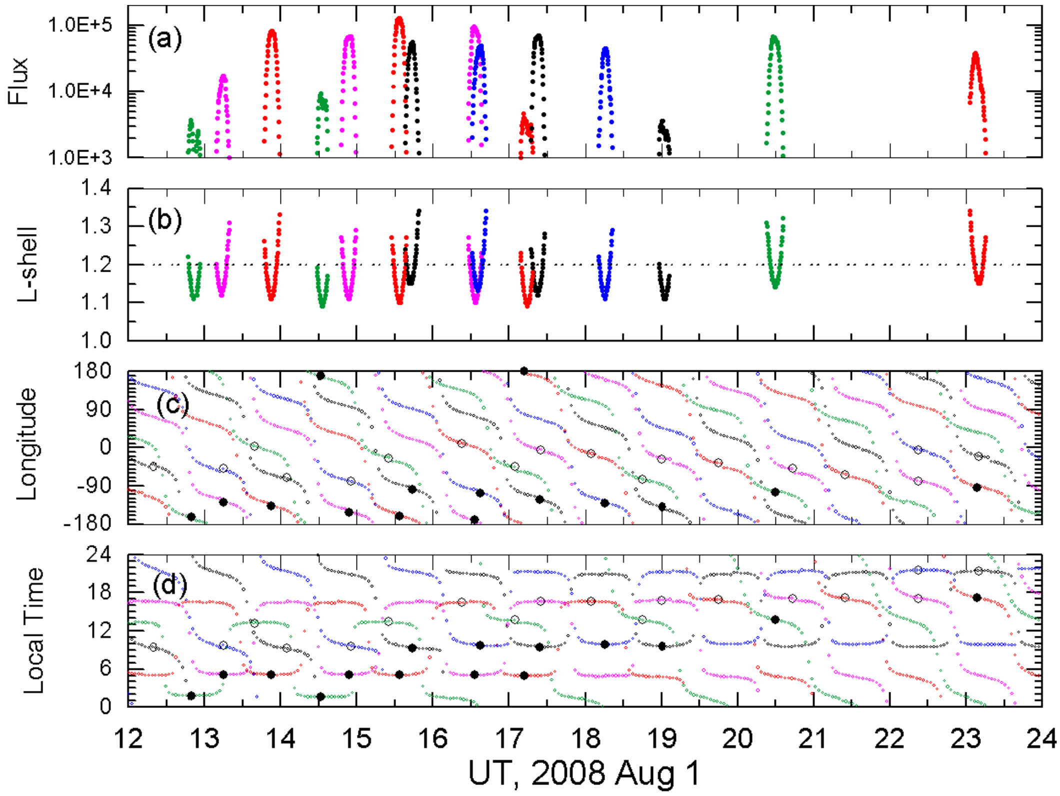

Figure 2. FEE enhancements on 1 August 2008: (a) fluxes of >30 keV electrons in units $(cm^2\ s\ sr)^{-1}$, (b) L-shell of enhancements, (c) longitude and (d) local time of peak fluxes (black circles). Measurements within the SAA area are indicated by the open circles. Colorful curves denote NOAA/POES satellites: P2 (black), P5 (pink), P6 (red), P7 (blue), and P8 (green). Horizontal dashed line at panel (b) depicts the lower edge of the inner radiation belt. FEE enhancements peak at the equator (minimal L-shells) that indicates a fast radial transport from the inner radiation belt.

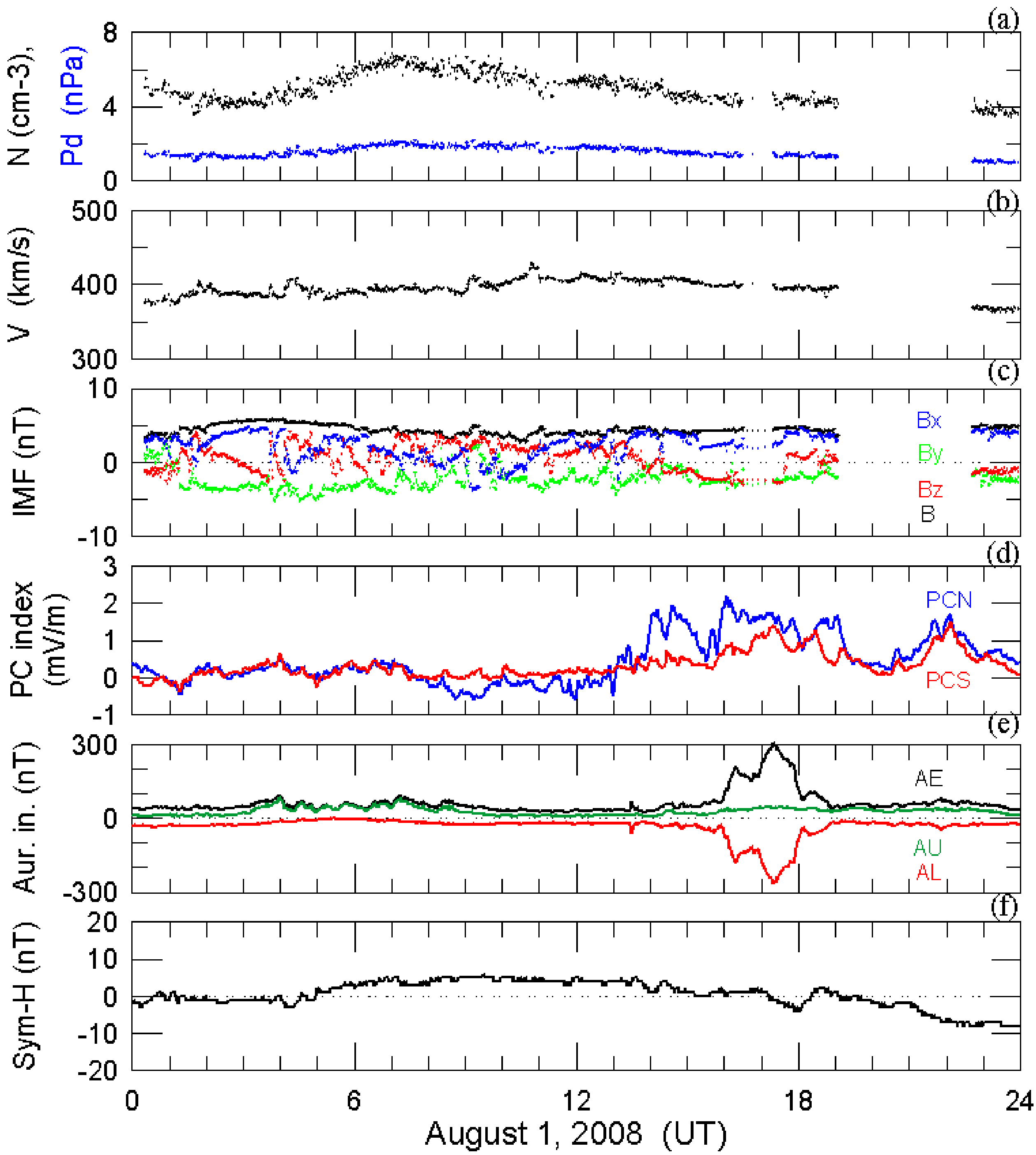

Figure 3. Solar wind parameters from OMNI data and geomagnetic indices on August 1, 2008. From top to bottom: (a) solar wind density (black) and dynamic pressure (blue), (b) solar wind speed, (c) interplanetary magnetic field (IMF) components Bx (blue), By (green), Bz (red) and magnitude B (black) in Geocentric Solar Magnetospheric (GMS) coordinates, (d) polar cap magnetic activity index PCN for northern (blue) and PCS for southern (red) hemispheres, (e) auroral electrojet index AE (black), AL (red), AU (green), and (f) storm time ring current variation index SYM-H. The shaded box denotes the time interval from 13 to 23 UT, when the nonstorm FEE enhancements were observed.

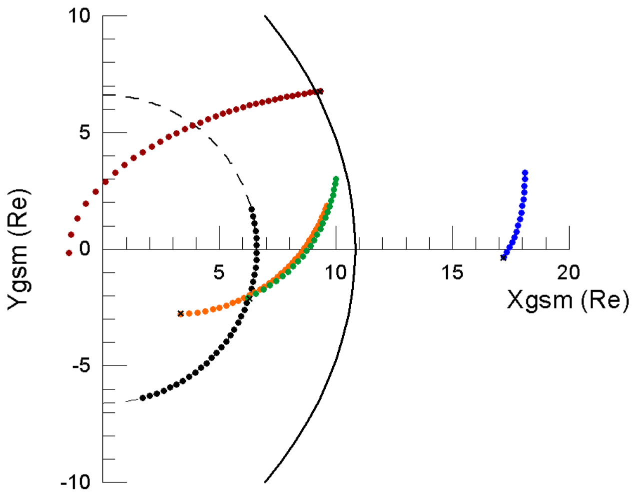

Figure 4. Spacecraft positions in GSM coordinates from 1200 to 1800 UT on August 1, 2018. The TH-C probe (blue) was in front of the subsolar bow shock. The TH-E (orange), TH-D (green), TH-B (brown), and GOES 12 (black) were located inside the dayside magnetosphere. The magnetopause position (black curve) was calculated using OMNI data for the upstream conditions at ~1600 UT following the model by Lin et al.'s (2010).

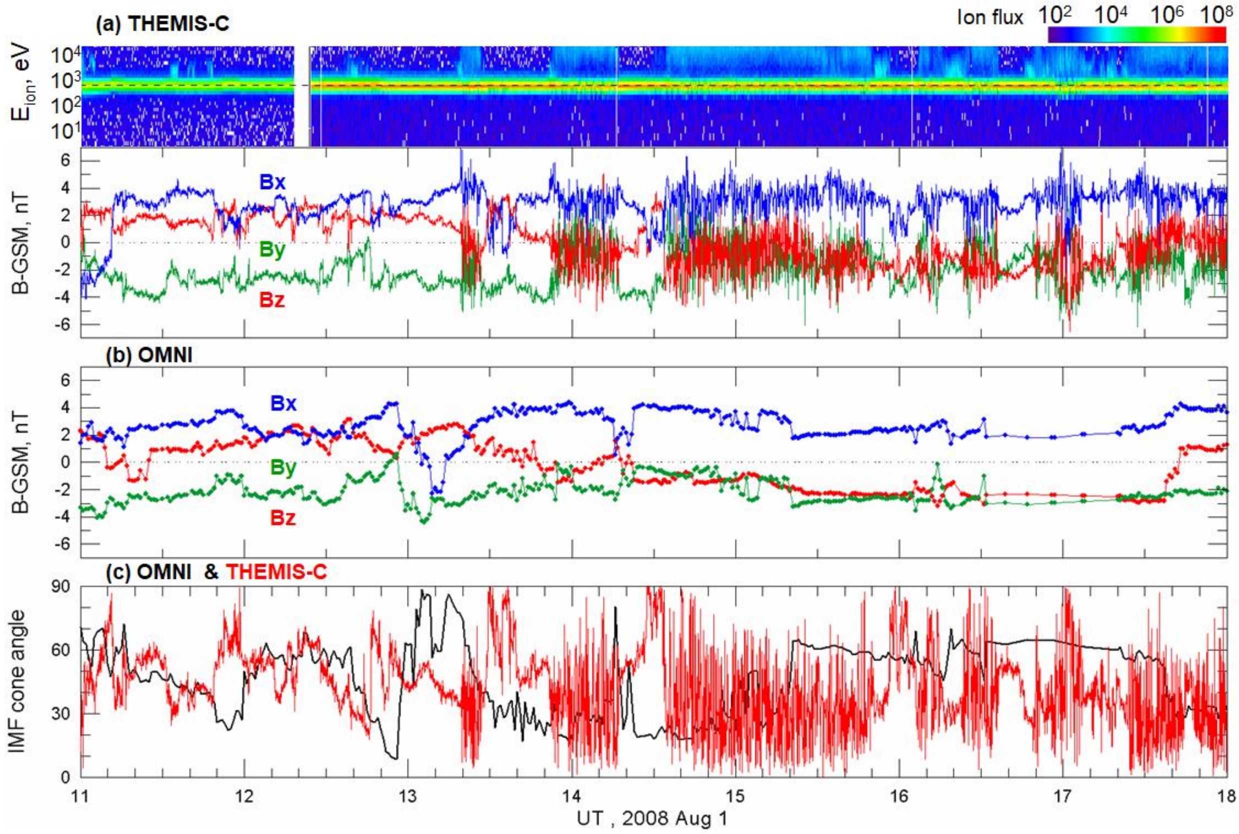

Figure 5. Observations of plasma and magnetic field on August 1, 2008. (a) Ion spectrogram (ion flux is in units of eV/cm^2 s sr eV) and IMF vector components in GSM coordinates measured by TH-C, (b) IMF vector components from OMNI data set, (c) IMF cone angles plotted for TH-C (red) and OMNI (black).

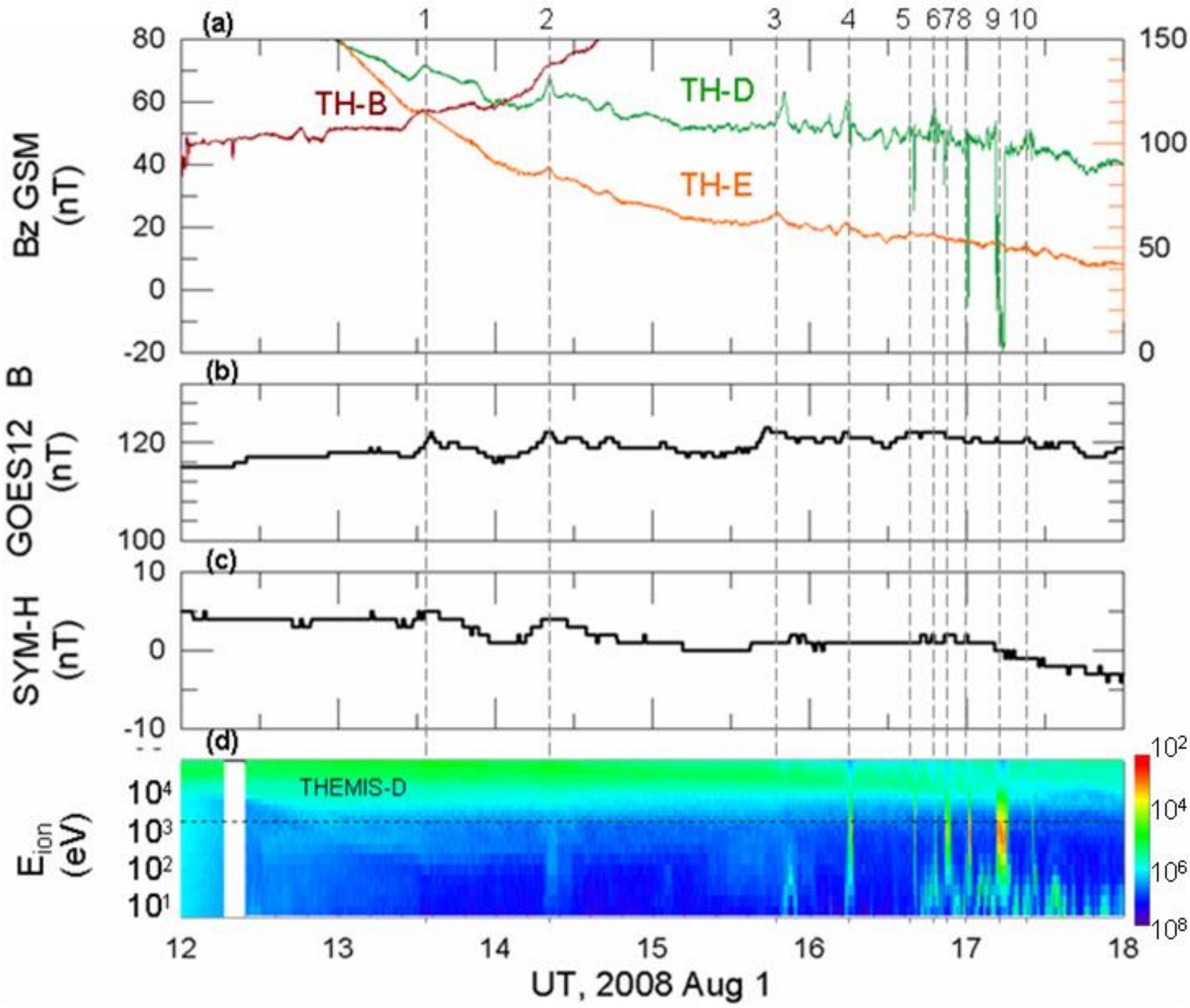

Figure 6. Satellite measurements of magnetic field and plasma in the dayside magnetosphere and geomagnetic activity. (a) The Bz-GSM components from THEMIS probes TH-B (brown), TH-E (orange), and TH-D (green). The left y-axis corresponds to the magnetic measurements from TH-B and TH-D, and the right y-axis to TH-E. (b) The magnetic field strength from GOES-12 (black); (c) the SYM-H index; and (d) the ion spectrogram from TH-D (ion flux is in units of eV/cm^2 s sr eV). Dashed lines, numbered from 1 to 10, indicate time moments of magnetic and plasma disturbances observed by THEMIS.

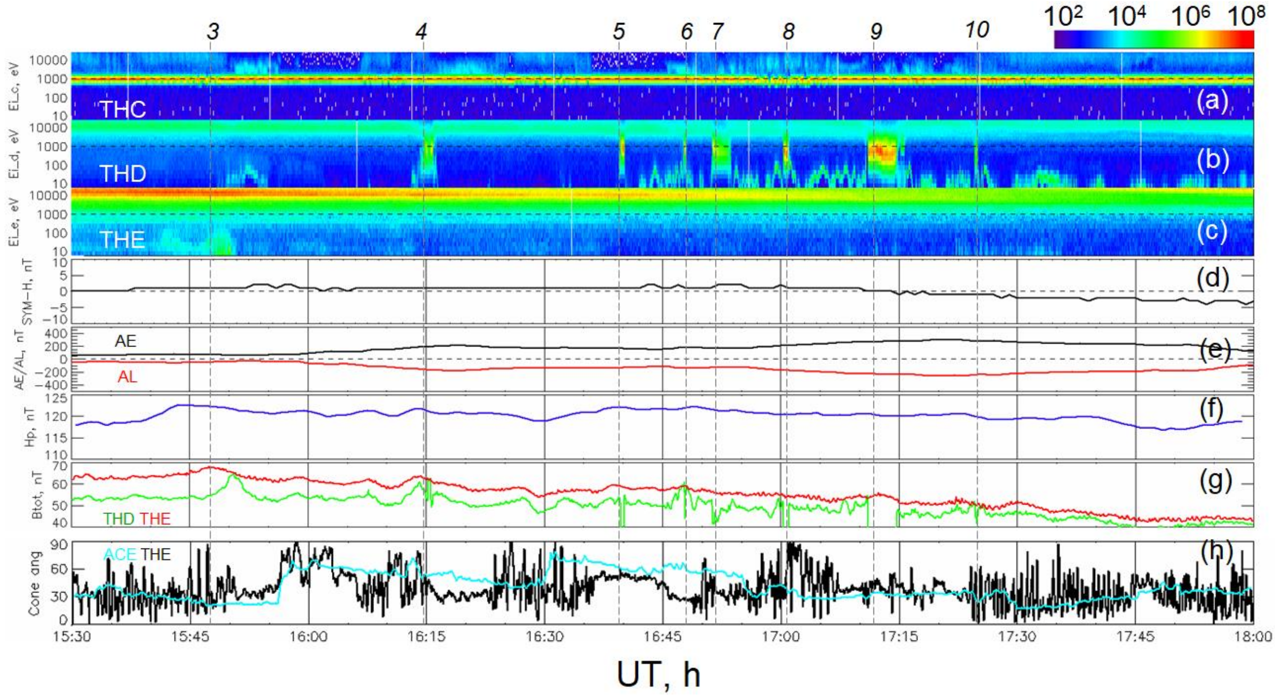

Figure 7. Observations of plasma and magnetic field at 1530-1800 UT on August 1, 2008: (a-c) ion spectrograms measured by TH-C, TH-D, and TH-E (ion flux is in units of eV/cm^2 s sr eV), (d) SYM-H index, (e) AE (black) and AL (red) indices, (f) horizontal magnetic field Hp detected by GOES 12 from 10 to 13 LT, (g) magnetic field strengths Btot from TH-D (green) and TH-E (red), (h) IMF cone angles for TH-C (black) and for the ACE upstream monitor (blue). The ACE measurements are delayed by 60 min. Dashed lines and numbers #4 - #10 mark magnetospheric disturbances with magnetosheath ion population observed in the magnetosphere.

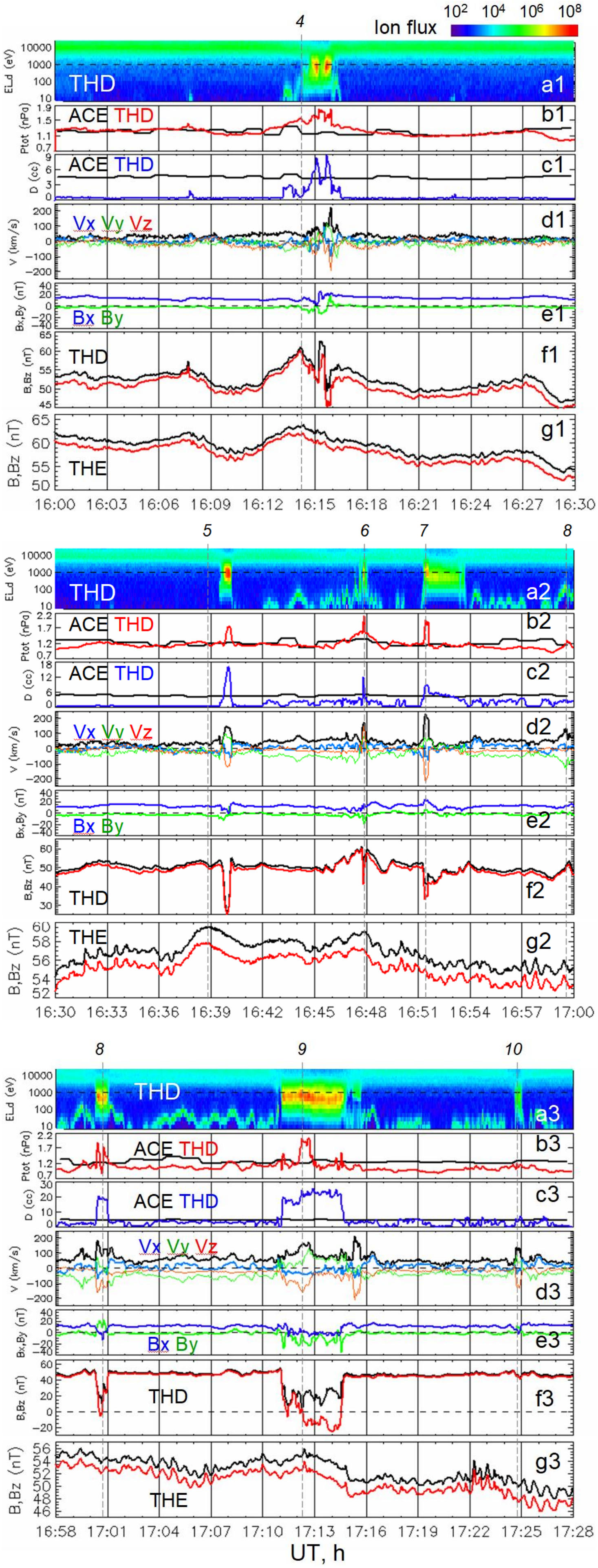
Ion flux
THD
ACE THD
Vx Vy Vz
Bx By
THE
UT, h

Figure 8. Observations of plasma and magnetic field during the intervals 1600 - 1630 UT, 1630 - 1700 UT and 1658 - 1728 UT on August 1, 2008. Panels show from top to bottom: (a) ion spectrogram from TH-D, (b) total pressure measured by the ACE upstream monitor (black) and TH-D (red), (c) plasma density measured by ACE (black) and TH-D (blue), (d) TH-D measurements of bulk velocity V (black) and its components in GSM coordinates Vx (blue), Vy (green) and Vz (red), (e) transversal components of magnetic field Bx (blue) and By (green) from TH-D, (f) magnitude B and Bz component of magnetic field from TH-D, (g) magnitude B and Bz component of magnetic field from TH-E. The magnetosheath plasma penetration is denoted by dashed lines and numbers #4 - #10.

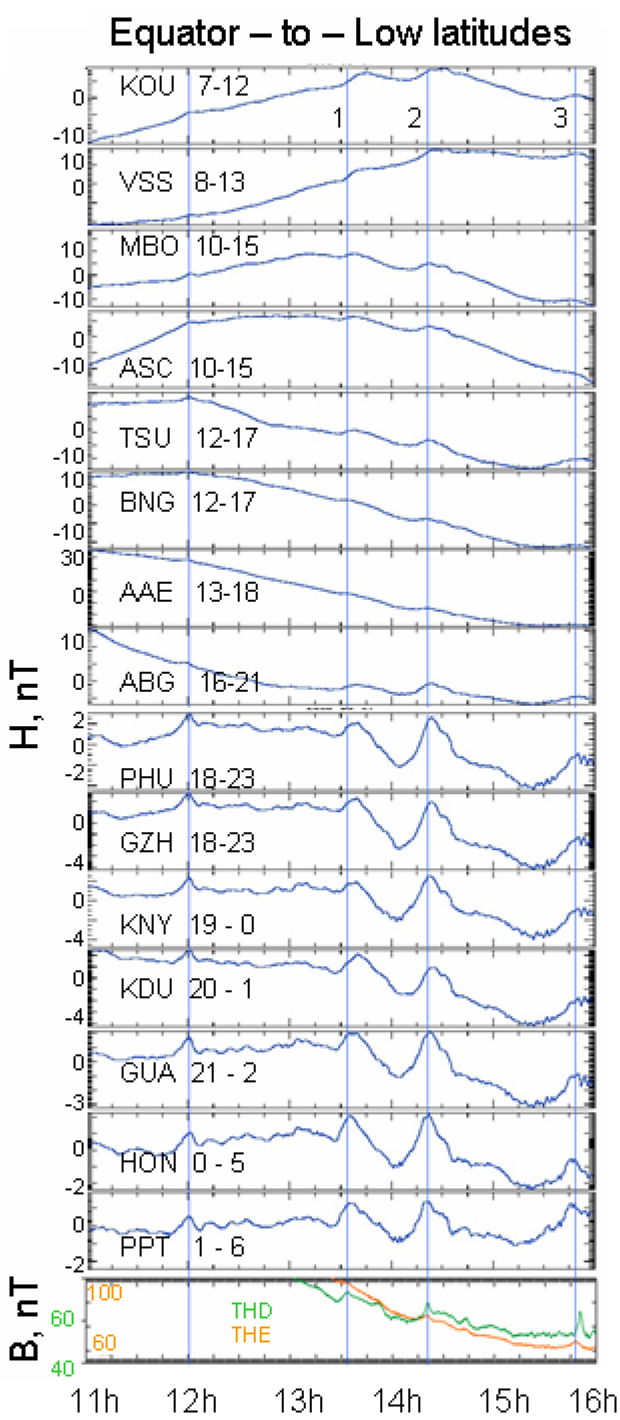

Figure 9. Relative variations in the horizontal component (H) of the geomagnetic field at low geomagnetic latitudes. Local time intervals are indicated near the station codes. The vertical lines depict time of the magnetic pulses at THEMIS (lines #1 - #3). Bottom panel shows magnetic field B measured by TH-E (orange) and by TH-D (green).

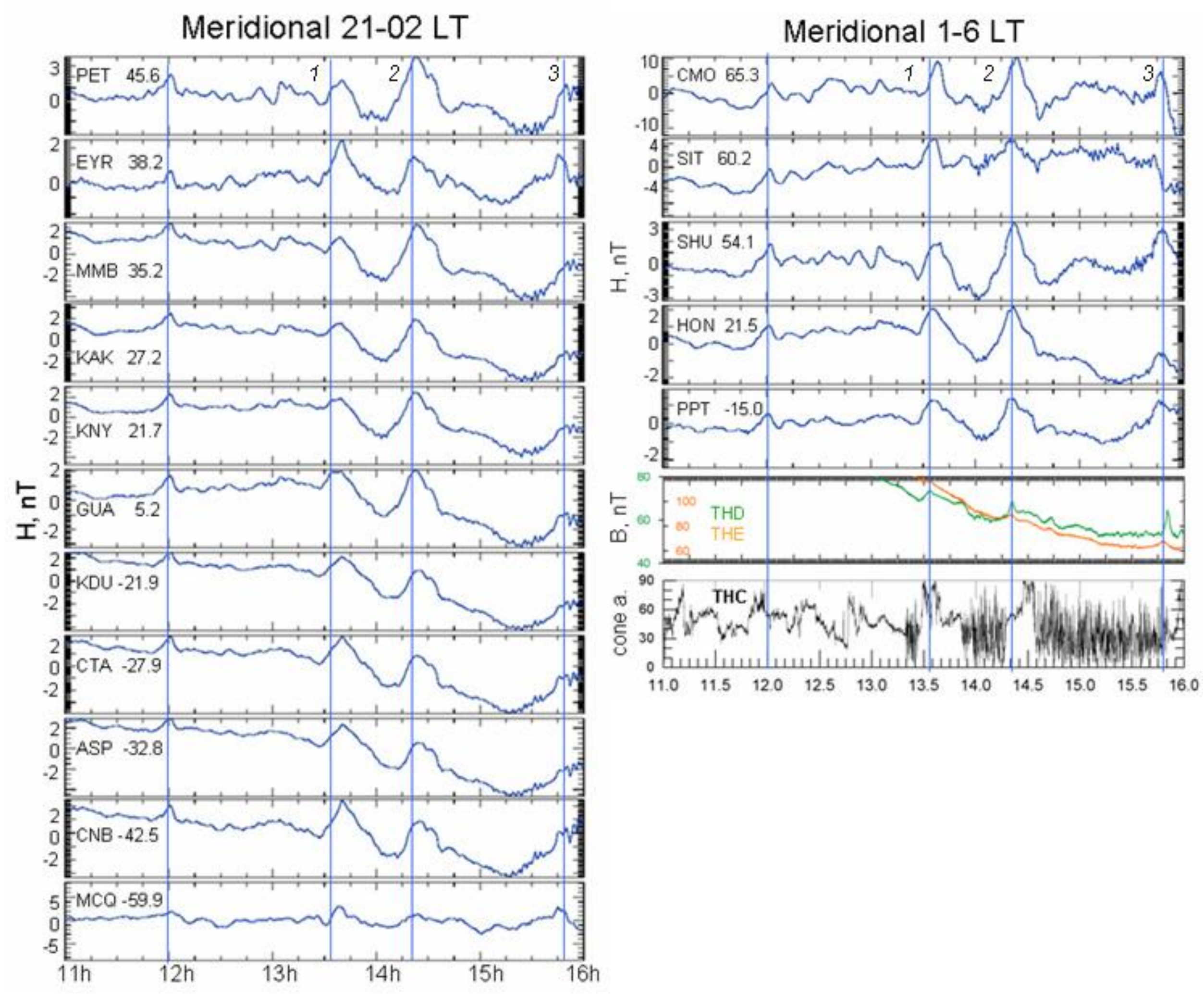

Figure 10. Relative variations in the horizontal component (H) of the geomagnetic field in the midnight (left) and predawn (right) sectors. The geomagnetic latitudes of the stations are indicated near station codes. The vertical lines depict time of the magnetic pulses at THEMIS.

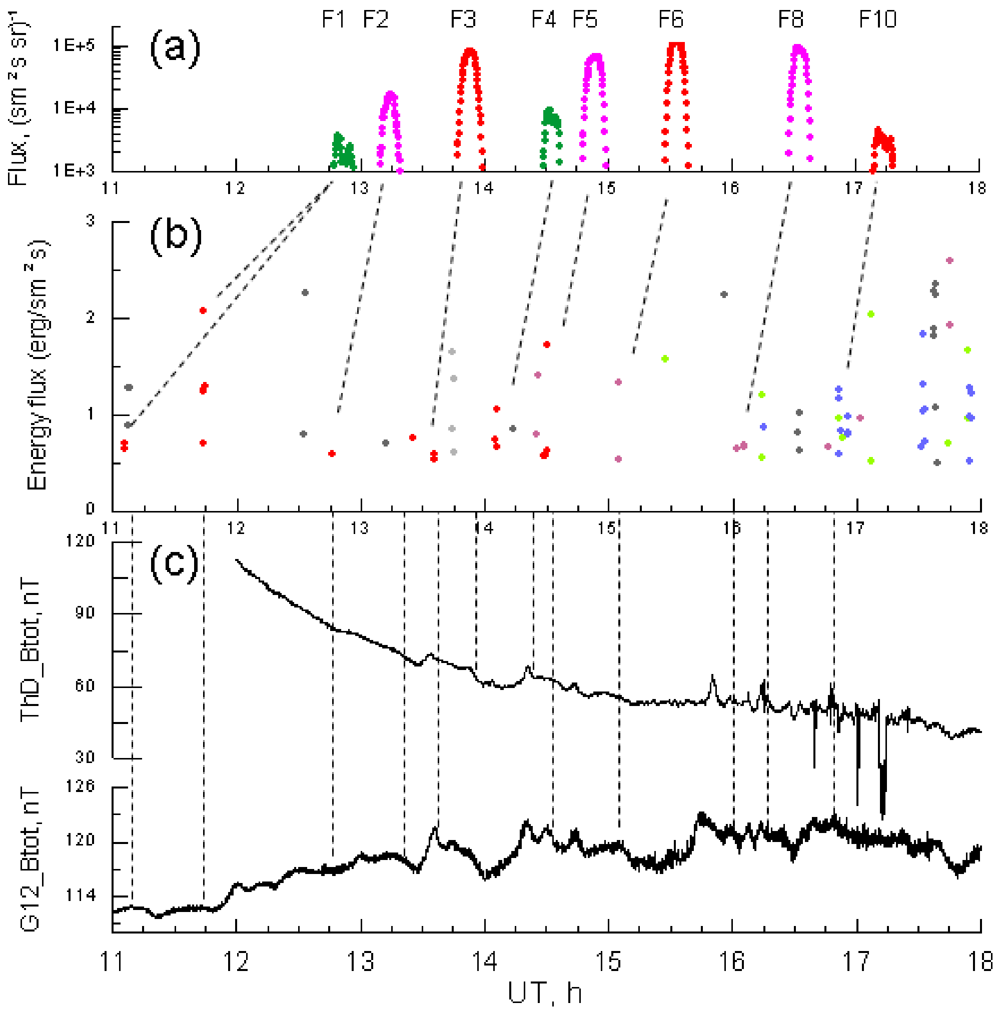

Figure 11. Dynamics of the geomagnetic field and particles on 1 August 2008: (a) FEE enhancements, (b) plasma precipitation at high latitudes, and dayside magnetic field perturbations observed by (c) GOES-12 and (d) THEMIS-D. The numbers indicate the FEE injections at ~2 and ~5 LT (see Table 1), colors for POES satellite are the same as in Figure 2. Plasma precipitations are shown for the energy flux above the threshold of 0.5 (erg/sm^2 s) and are grouped in LT: 23 – 24 LT (light gray), 0 – 2 LT (gray), 5 – 6 LT (blue), 12.5 - 15 LT (red points), 15 – 16 LT (violet), and 19.5 – 21.5 LT (green).